Article

Cancer Cell

Fibroblast Heterogeneity and Immunosuppressive Environment in Human Breast Cancer

Graphical Abstract

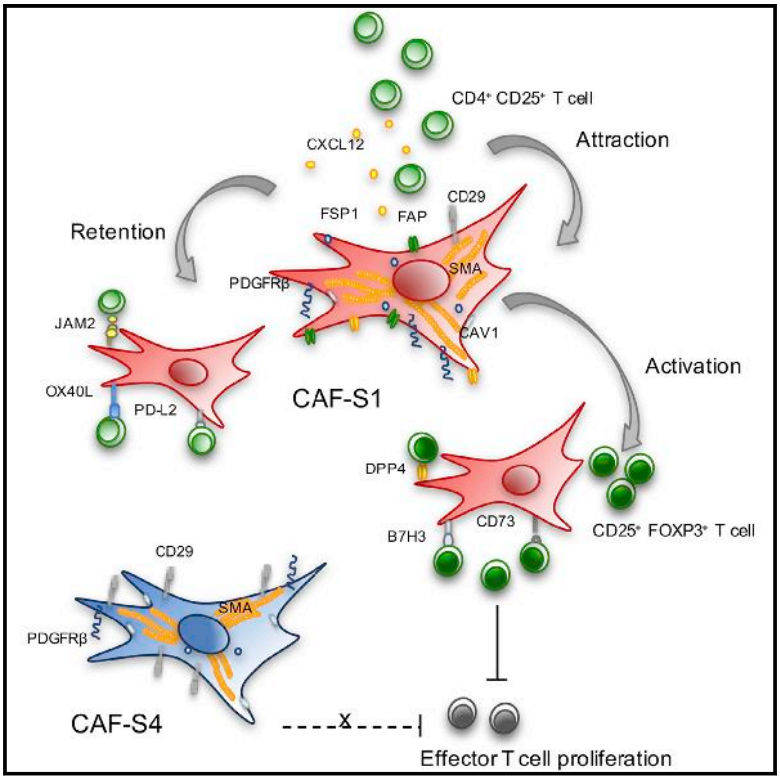

Highlights

- Four CAF subsets identified in breast cancer accumulate differently in BC subtypes
- CAF-S1 subset is associated with an immunosuppressive microenvironment
- CAF-S1 cells attract and retain $CD4^+CD25^+$ T cells through OX40L, PD-L2, and JAM2
- CAF-S1 cells increase $CD25^+FOXP3^+$ T lymphocytes, through B7H3, DPP4, and CD73

Authors

Ana Costa, Yann Kieffer, Alix Scholer-Dahirel, ..., Vassili Soumelis, Anne Vincent-Salomon, Fatima Mechta-Grigoriou

Correspondence

fatima.mechta-grigoriou@curie.fr

In Brief

Costa et al. identify four subsets of carcinoma-associated fibroblasts (CAF) in breast cancer. CAF-S1 promotes an immunosuppressive microenvironment by recruiting $CD4^+CD25^+$ T cells, via secreting CXCL12, and promoting their differentiation to Tregs and survival, via expressing T cell interacting proteins.

Costa et al., 2018, Cancer Cell *33*, 463–479
March 12, 2018
https://doi.org/10.1016/j.ccell.2018.01.011

CellPress

Cancer Cell
Article

Fibroblast Heterogeneity and Immunosuppressive Environment in Human Breast Cancer

Ana Costa,[1,2] Yann Kieffer,[1,2,7] Alix Scholer-Dahirel,[1,2,3,7] Floriane Pelon,[1,2,7] Brigitte Bourachot,[1,2] Melissa Cardon,[1,2] Philemon Sirven,[1,2,3] Ilaria Magagna,[1,2] Laetitia Fuhrmann,[5] Charles Bernard,[1,2] Claire Bonneau,[1,2] Maria Kondratova,[6] Inna Kuperstein,[6] Andrei Zinovyev,[6] Anne-Marie Givel,[1,2] Maria-Carla Parrini,[4] Vassili Soumelis,[3] Anne Vincent-Salomon,[5] and Fatima Mechta-Grigoriou[1,2,8,*]

[1]Institut Curie, Stress and Cancer Laboratory, Equipe labelisée Ligue Nationale Contre le Cancer, PSL Research University, 26, rue d'Ulm, 75005 Paris, France
[2]Inserm, U830, Paris 75005, France
[3]Institut Curie, Integrative Biology of Human Dendritic Cells and T Cells Laboratory, PSL Research University, Inserm, U932, 26, rue d'Ulm, 75005 Paris, France
[4]Analysis of Transduction Pathway, Institut Curie, Inserm, U830, PSL Research University, 26 rue d'Ulm, Paris 75005, France
[5]Department of Pathology, Institut Curie Hospital Group, 26, rue d'Ulm, 75248 Paris, France
[6]Institut Curie, PSL Research University, Inserm, U900, Mines Paris Tech, Paris 75005, France
[7]These authors contributed equally
[8]Lead Contact
*Correspondence: fatima.mechta-grigoriou@curie.fr
https://doi.org/10.1016/j.ccell.2018.01.011

SUMMARY

Carcinoma-associated fibroblasts (CAF) are key players in the tumor microenvironment. Here, we characterize four CAF subsets in breast cancer with distinct properties and levels of activation. Two myofibroblastic subsets (CAF-S1, CAF-S4) accumulate differentially in triple-negative breast cancers (TNBC). CAF-S1 fibroblasts promote an immunosuppressive environment through a multi-step mechanism. By secreting CXCL12, CAF-S1 attracts $CD4^+CD25^+$ T lymphocytes and retains them by OX40L, PD-L2, and JAM2. Moreover, CAF-S1 increases T lymphocyte survival and promotes their differentiation into $CD25^{High}FOXP3^{High}$, through B7H3, CD73, and DPP4. Finally, in contrast to CAF-S4, CAF-S1 enhances the regulatory T cell capacity to inhibit T effector proliferation. These data are consistent with FOXP3+ T lymphocyte accumulation in CAF-S1-enriched TNBC and show how a CAF subset contributes to immunosuppression.

INTRODUCTION

Breast cancer (BC) is a frequent cancer in women and remains a major cause of cancer-associated death in western countries, despite attempts to provide effective therapies. Even though the mortality rate for BC is overall slowly declining with the improvement of both early detection and therapies, only limited success has been achieved in case of advanced cancers. Based on histopathological analysis, BC has been defined as a heterogeneous disease classified into three main subtypes: luminal (Lum), HER2, and triple-negative (TN), which have been complemented by gene expression profiling (Perou et al., 2000; Sorlie et al., 2001). Tumors are complex ecologies that are affected by numerous stromal factors that dampen or enhance the effects of genetic epithelial alterations. While normal fibroblasts suppress tumor formation (Dotto et al., 1988), cancer-associated fibroblasts (CAFs) enhance tumor phenotypes, notably cancer cell proliferation and invasion, neo-angiogenesis, inflammation, and extracellular matrix (ECM) remodeling (Costa et al., 2014; Gascard and Tlsty,

Significance

Fibroblast heterogeneity has been recognized, yet the absence of precise markers to identify CAFs makes their identity unclear and studies difficult to compare. Our work provides an advance in the field by the identification of four CAF subsets that accumulate differentially in normal tissue and in BC subtypes. Although CAFs were recently associated with immunosuppression, the mechanism involved was unknown. Our findings describe how a specific CAF subset, named CAF-S1, promotes immunosuppression through a multi-step mechanism and decipher the different CAF-S1 molecules involved at each step. Overall, we suggest that BC tumors enriched in CAF-S1 could acquire resistance to immunotherapies, and CAF-S1 molecules identified here provide potential targets that can pave the way for treatment strategies.

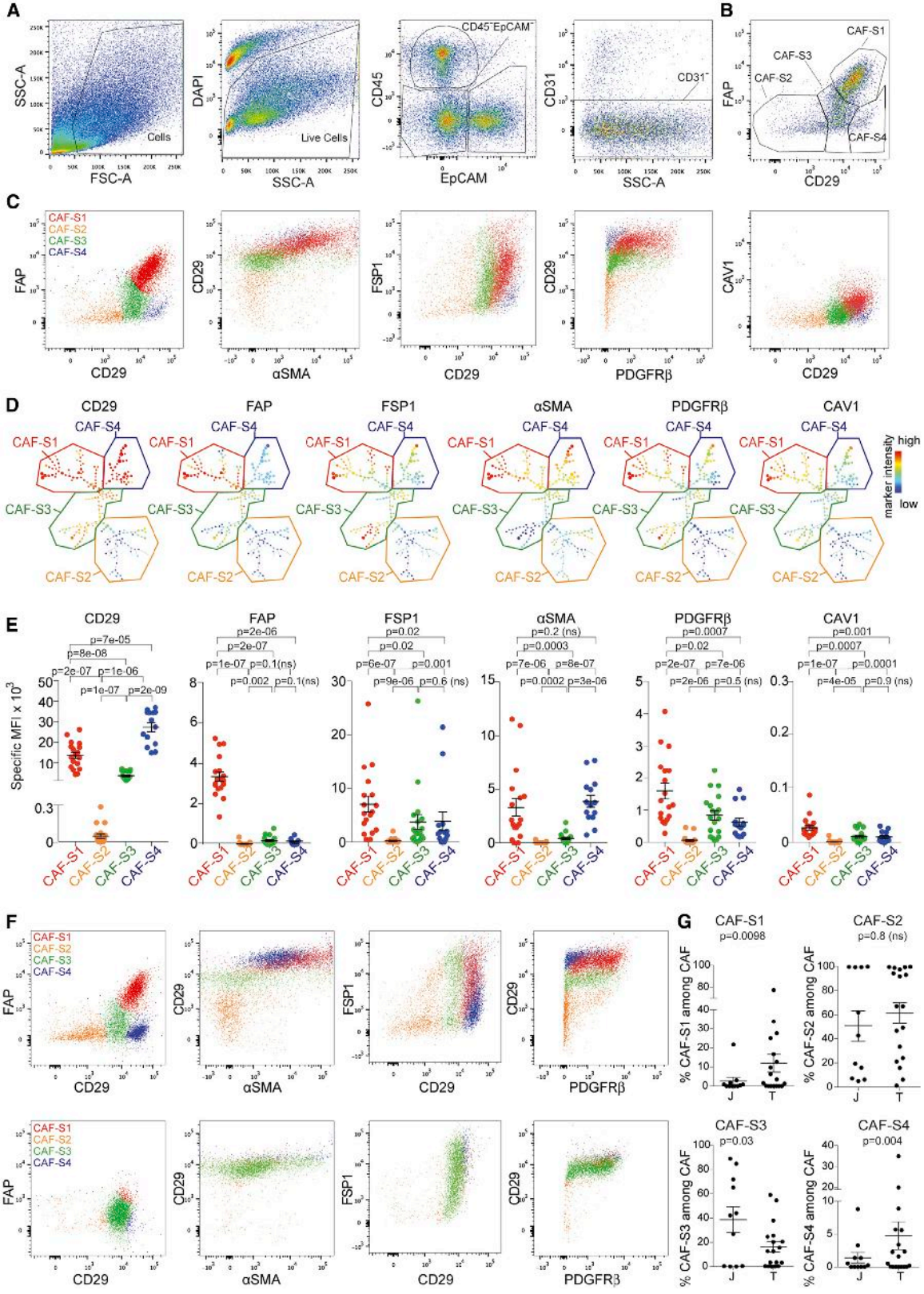

(legend on next page)

2016; Gentric et al., 2016). Although it remains controversial whether CAFs prevent or drive cancer cell invasion (Ozdemir et al., 2014), tumor-promoting activities of CAFs have been widely described (Olumi et al., 1999; Allinen et al., 2004; Orimo et al., 2005; Kalluri and Zeisberg, 2006; Erez et al., 2010; Toullec et al., 2010; Hammer et al., 2017). In human breast tumors, the abundance of stromal myofibroblasts (i.e., α-smooth muscle actin [αSMA]-positive fibroblasts) is associated with aggressive adenocarcinomas and predicts human disease recurrence (Toullec et al., 2010; Benyahia et al., 2017). In addition, CAFs have been shown to contribute to drug resistance (Straussman et al., 2012; Paulsson et al., 2017) and to reduce anti-tumor immunity (Kraman et al., 2010; Tan et al., 2011; Feig et al., 2013; Denton et al., 2014; Ruhland et al., 2016; Yang et al., 2016). Several studies in immunocompetent mice showed that FAP (fibroblast activation protein α1)-positive CAFs drive immunosuppression and resistance to anti-PD-L1 immunotherapy. Yet it remains unclear whether this CAF-mediated immunosuppressive function is relevant in human tumors and if so, what are the mechanisms involved.

Although CAFs are the most prominent stromal components, characterizing their heterogeneity in human cancers is far from complete. Several markers, such as αSMA, FAP, integrin β1/CD29, S100-A4/FSP1 (fibroblast-specific protein 1), PDGFRβ (platelet-derived growth factor receptor-β), and CAV1 (caveolin 1) have been studied individually in the past years. Indeed, numerous studies used αSMA to stain myofibroblasts in human tumors and showed that they accumulate in BC of poor prognosis (Toullec et al., 2010). Moreover, recently, two CAF subpopulations with different levels of αSMA have been identified in pancreatic cancers, with one being myofibroblastic and the other one pro-inflammatory (Ohlund et al., 2017). In addition to αSMA, high stromal PDGFRβ expression was associated with shorter BC patient survival (Paulsson et al., 2014). Furthermore, FAP was shown to be abundantly expressed in the stroma of BC. Such expression either showed no link with clinicopathological factors (Tchou et al., 2013) or, in contrast, has been associated with longer survival (Ariga et al., 2001). Finally, the clinical significance of either CAV1 or FSP1 expression in stroma has been demonstrated in BC, although with some conflicting information on patient survival (Rudland et al., 2000; Lee et al., 2004; Goetz et al., 2011; Simpkins et al., 2012). A first study analyzing αSMA, PDGFRβ, and S100A4/FSP1 together was performed in mouse pancreatic and BCs and showed that they exhibit a differential expression in CAFs (Sugimoto et al., 2006). Here, we analyzed CAF heterogeneity in human BC and investigated the link of this heterogeneity with immunosuppression.

RESULTS

Identification of Four CAF Subsets in Human BC

To define CAF heterogeneity in human BC, we first performed a detailed characterization of CAFs using multicolor flow cytometry (fluorescence-activated cell sorting [FACS]). To do so, we used CD45, EPCAM, and CD31 markers to exclude hematopoietic, epithelial, and endothelial cells, respectively (Figure 1A), and performed the concomitant analysis of six fibroblast markers (FAP, integrin β1/CD29, αSMA, S100-A4/FSP1, PDGFRβ, and CAV1) (Figures 1B and 1C). The fresh BC samples studied (FACS prospective cohort) included BC patients at time of surgery prior to any treatment, conditions in favor of Lum BC patient inclusion (Table S1). We observed CAFs constitute a heterogeneous cellular population (Figure 1B). We established a gating strategy that enabled us to distinguish four different CAF subpopulations in BC, according to the expression levels of CD29, FAP, αSMA, PDGFRβ, FSP1, and CAV1 (Figures 1B and 1C). These four CAF subpopulations were referred to as CAF-S1 (red), CAF-S2 (orange), CAF-S3 (green), and CAF-S4 (blue). We next analyzed FACS data obtained with the six CAF markers through an unbiased method, CytoSPADE (Qiu et al., 2011) that organizes cells into hierarchies of related phenotypes. The tree built by applying this algorithm to FACS data confirmed the existence of the four CAF subsets in BC (Figure 1D). We evaluated the redundancy between the different markers by repeating the CytoSPADE analysis in absence of each of the six markers (Figure S1A). Changes in the input data (lack of one stromal marker) significantly affected the global structure of the tree (Figure S1A), suggesting that these markers are not redundant and bring additive information. The CAF-S1 subset was characterized by high expression of the six markers except CAV1, while CAF-S2 fibroblasts exhibited low expression of all these markers (Figure 1E). In contrast to CAF-S2 and CAF-S3 subsets, both CAF-S1 and CAF-S4 fibroblasts expressed αSMA and could be considered as myofibroblasts (Figures 1C–1E). In addition, CAF-S1 subset was the only one to be positive for FAP and CAF-S4 cells exhibited the highest expression of CD29 compared with the other CAF subsets. Furthermore, both CAF-S3 and CAF-S4 subsets were positive for PDGFRβ and FSP1. CAV1 exhibited very low staining by FACS in all CAF subsets (Figure 1E). In conclusion, these CAF subsets can be defined as follows: CAF-S1: $CD29^{Med}$ FAP^{Hi} $FSP1^{Low-Hi}$ αSMA^{Hi} $PDGFR\beta^{Med-Hi}$ $CAV1^{Low}$; CAF-S2: $CD29^{Low}$ FAP^{Neg} $FSP1^{Neg-Low}$ αSMA^{Neg} $PDGFR\beta^{Neg}$ $CAV1^{Neg}$; CAF-S3: $CD29^{Med}$ FAP^{Neg} $FSP1^{Med-Hi}$ $\alpha SMA^{Neg-Low}$

Figure 1. Identification of CAF Subsets in Human BC

(A–C) Gating strategy to identify CAF subsets in BC by FACS shown for one representative tumor. Cells gated on $DAPI^-$, $EPCAM^-$, $CD45^-$, and $CD31^-$, to exclude dead, epithelial, hematopoietic, and endothelial cells, respectively (A). (B and C) Live $EPCAM^-$, $CD45^-$, and $CD31^-$ cells analyzed with CD29, FAP, αSMA, FSP1, PDGFRβ, and CAV1 markers. Representative FACS plot showing four CAF subsets (B). Representative FACS plots of the six CAF markers (C).

(D) CytoSpade trees annotated for each CAF marker expression (n = 20). Colors show staining intensities of each marker; node size is proportional to the number of cells with similar CAF marker expression.

(E) Specific mean fluorescence intensity (MFI) for each marker per CAF subset. Each dot represents one patient (n = 18). Data are mean ± SEM. p values from Mann-Whitney test.

(F) FACS plots of CD29, FAP, αSMA, FSP1, and PDGFRβ from a representative breast tumor; different from (A) (top) and its corresponding juxta-tumor (bottom).

(G) Quantification of CAF subset among total CAFs in tumors (T) and corresponding juxta-tumors (J) (n = 18). Data are mean ± SEM. p values from Wilcoxon signed rank test. See also Figure S1, Tables S1 and S2.

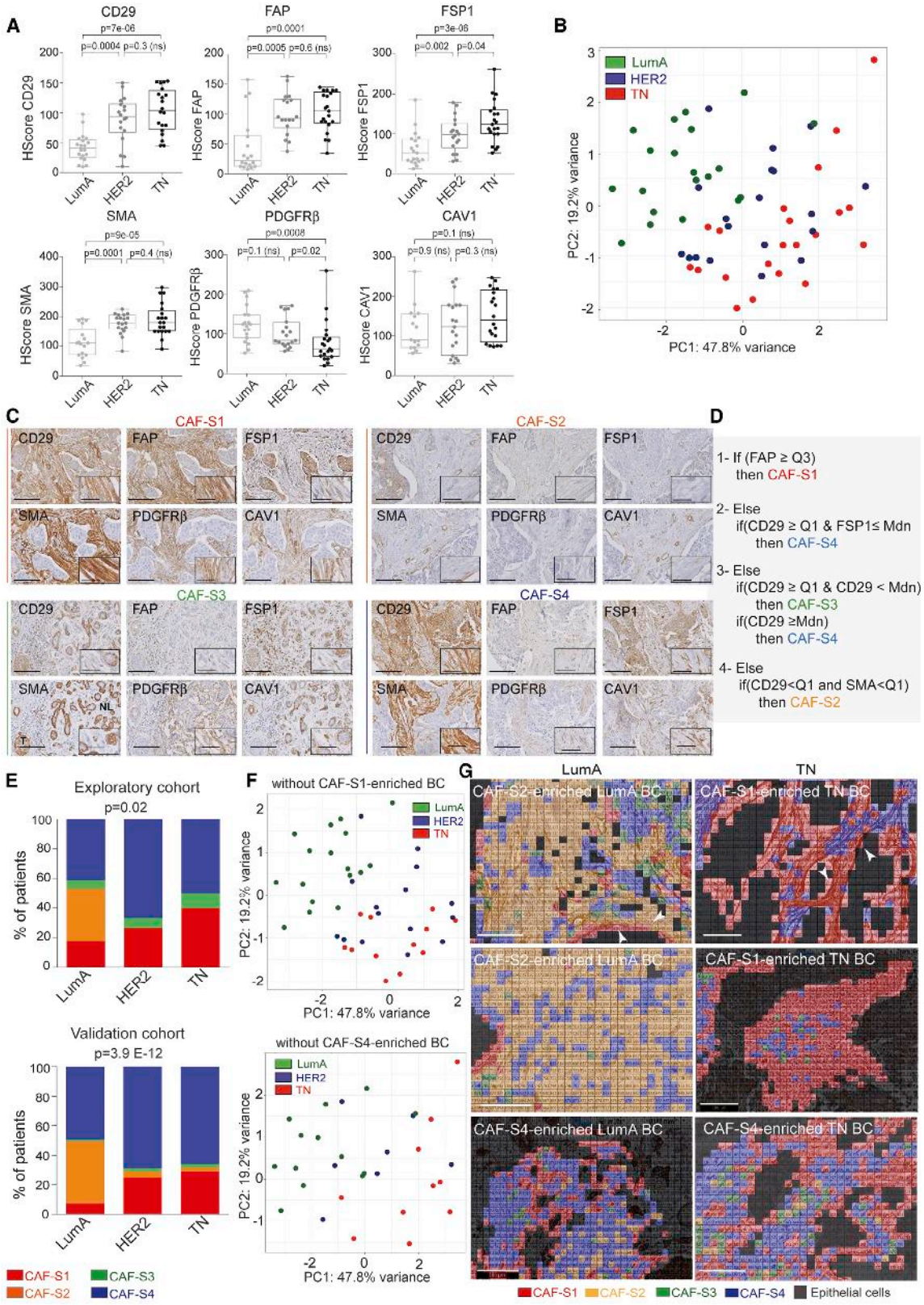

(legend on next page)

PDGFRβ^{Med} CAV1$^{Neg-Low}$; CAF-S4: CD29^{Hi} FAP^{Neg} FSP1$^{Low-Med}$ αSMA^{Hi} PDGFRβ$^{Low-Med}$ CAV1$^{Neg-Low}$. As the CAF-S2 subset was low or negative for the six CAF markers tested by FACS, we could not rule out that CAF-S2 cells might be another cell type. Still, immunohistochemistry (IHC) analyses on serial tumor sections (see below) confirmed the existence of CAF-S2 devoid of the six stromal markers analyzed. We did not observe any association between CAF subsets and clinical features of the FACS prospective cohort (Table S2), most probably because this cohort was mainly composed by Lum BC patients. In contrast, we observed that the four CAF subsets accumulated differentially in tumors compared with their corresponding juxta-tumors, defined as healthy tissues by pathologists (Figures S1B, 1F, and 1G). Indeed, both CAF-S1 and CAF-S4 subsets were preferentially detected in tumors, while CAF-S3 subset was significantly associated with juxta-tumors and CAF-S2 equally distributed in the two compartments (Figures S1B, 1F, and 1G). Thus, based on the detection of several fibroblastic markers by FACS, we identified four distinct CAF subsets in human BC that accumulate differentially in tumors and juxta-tumors.

Repartition and Spatial Distribution of CAF Subsets in BC Subtypes

We next aimed at confirming the existence of four CAF subsets in BC using an independent method. We performed IHC on two independent cohorts composed of the three molecular BC subtypes, LumA, HER2, and TNBC (retrospective exploratory and validation cohorts; Table S1). All fibroblast markers stained CAFs, as expected, but some of them (such as CD29 and FSP1) also stained epithelial cells (Figure S2A). We thus concentrated our analysis on stroma, and quantified staining of each marker in CAFs (Figure 2A). The histological scores (HScores) evaluated for each marker revealed heterogeneity between BC subtypes. LumA BC exhibited the lowest HScores for the majority of the fibroblast markers compared with HER2 and TNBC, the later showing the highest levels of CD29, FAP, FSP1, and αSMA compared with LumA (Figure 2A). As the percentage of stroma was higher in LumA BC compared with HER2 and TNBC (Figure S2B), we reported CAF marker HScores to the proportion of stroma and confirmed that HScores remained higher for CD29 and FAP in TNBC, compared with LumA BC (Figure S2C). We next performed an unsupervised principal-component analysis (PCA) on CAF marker HScores (Figure 2B). Histological scoring of the six CAF markers enabled us to differentiate BC subtypes, in particular LumA from TNBC (Figure 2B). In histological sections, we have been able to distinguish BC areas enriched in one particular CAF subset (Figures 2C and S2D). We developed a decision tree based on the distribution of the CAF marker intensities (Figure 2D and the STAR Methods) and defined the CAF subset, which was preponderant in each tumor (Figure 2E). We validated the robustness of the decision tree by performing a sensitivity analysis (applying Monte Carlo one-variable-at-a-time approach). Even a large 2-fold uncertainty misclassified only a minor fraction of samples, with a maximum of 14% misclassification rate observed for assigning the CAF-S4 subtype (Figures S2E–S2G), indicating the constructed classifier allows robust CAF subtyping. The CAF-S3 subset, mainly detected in juxta-tumors (Figures 1F and 1G), accumulated in a small number of tumors and was equally distributed in the three BC subtypes (Figure 2E). Most LumA tumors were enriched in CAF-S2 cells, HER2 in CAF-S4 and TN either in CAF-S1 or in CAF-S4 (Figure 2E; Table S2; retrospective cohort). Indeed, although HER2 BC accumulated mostly the CAF-S4 subset, CAF-S4 cells were also detected in LumA and TNBC. Moreover, while CAF-S1 and CAF-S4 fibroblasts are both positive for αSMA, we could distinguish two subgroups of TNBC based on CAF-S1 or CAF-S4 subset composition (Figure 2E; Table S2). We plotted the same PCA as in Figure 2B without CAF-S4- or CAF-S1-enriched BC (Figure 2F) and observed that CAF-S4-enriched TNBC were mixed with CAF-S4-enriched HER2 BC, while CAF-S1-enriched TNBC or CAF-S1-enriched HER2 BC remained clustered (Figure 2F). While none of the CAF subset was indicative of BC patient survival, we found a significant association between CAF subsets and histological grade, BC subtypes and treatment by chemotherapy (Table S2). Finally, we developed an image analysis tool that combined spatial registration and joint computational analysis of serial consecutive IHC sections (see the STAR Methods). We applied the CAF decision tree algorithm and generated maps of CAF subsets at cellular level, where we visualized CAF subset spatial distribution in tumors (Figures 2G and S2H–S2M). Representative pictures of CAF subset maps confirmed the overall enrichment in CAF-S2 in LumA tumors and accumulation of CAF-S1 and CAF-S4 in TNBC (Figures 2G and S2N–S2P). Moreover, CAF-S1 fibroblasts were also preferentially detected close to epithelial tumor cells (represented in dark gray) (Figure 2G, arrows). Taken together, by studying independent cohorts of BC patients and using two different methods, we identified four CAF subsets that accumulate differentially in BC subtypes and exhibit specific spatial distribution.

Figure 2. Repartition and Spatial Distribution of CAF Subsets in Human BC

(A) Histological scores (HScores) per CAF marker. Each dot represents one CAF HScore per patient sample (n = 60). Data are median ± min to max. p values from Student's t test (FSP1 and αSMA) or Mann-Whitney test (CD29, FAP, PDGFRβ, and CAV1).

(B) Principal-component analysis (PCA) based on HScores of the six CAF markers in BC (n = 60).

(C) Representative staining of CD29, FAP, FSP1, αSMA, PDGFRβ, and CAV1 in serial BC sections showing areas enriched in CAF-S1, CAF-S2, CAF-S3, or CAF-S4. Scale bars, 100 μm, 25 μm (inset). T, tumor cells; NL, normal lobules.

(D) Decision tree defining CAF identity based on quartile (Q) and median (Mdn) distribution of CAF markers. Thresholds (Mdn, Q) and decisions were first established from FACS data and next applied to IHC data.

(E) Repartition of CAF subset enrichment in BC in the exploratory (n = 52) and validation (n = 188) cohorts. The predominant CAF subset defines the CAF subset enrichment per tumor. Data are shown as percentage of BC. p values from Fisher's exact test.

(F) Same PCA analysis as in (B) excluding CAF-S1 or CAF-S4.

(G) Maps of CAF subsets at cellular scale in LumA (left) and TN (right) BC sections. White arrows indicate CAF-S1 close to tumor cells. Scale bars, 100 μm. See also Figure S2, Tables S1 and S2.

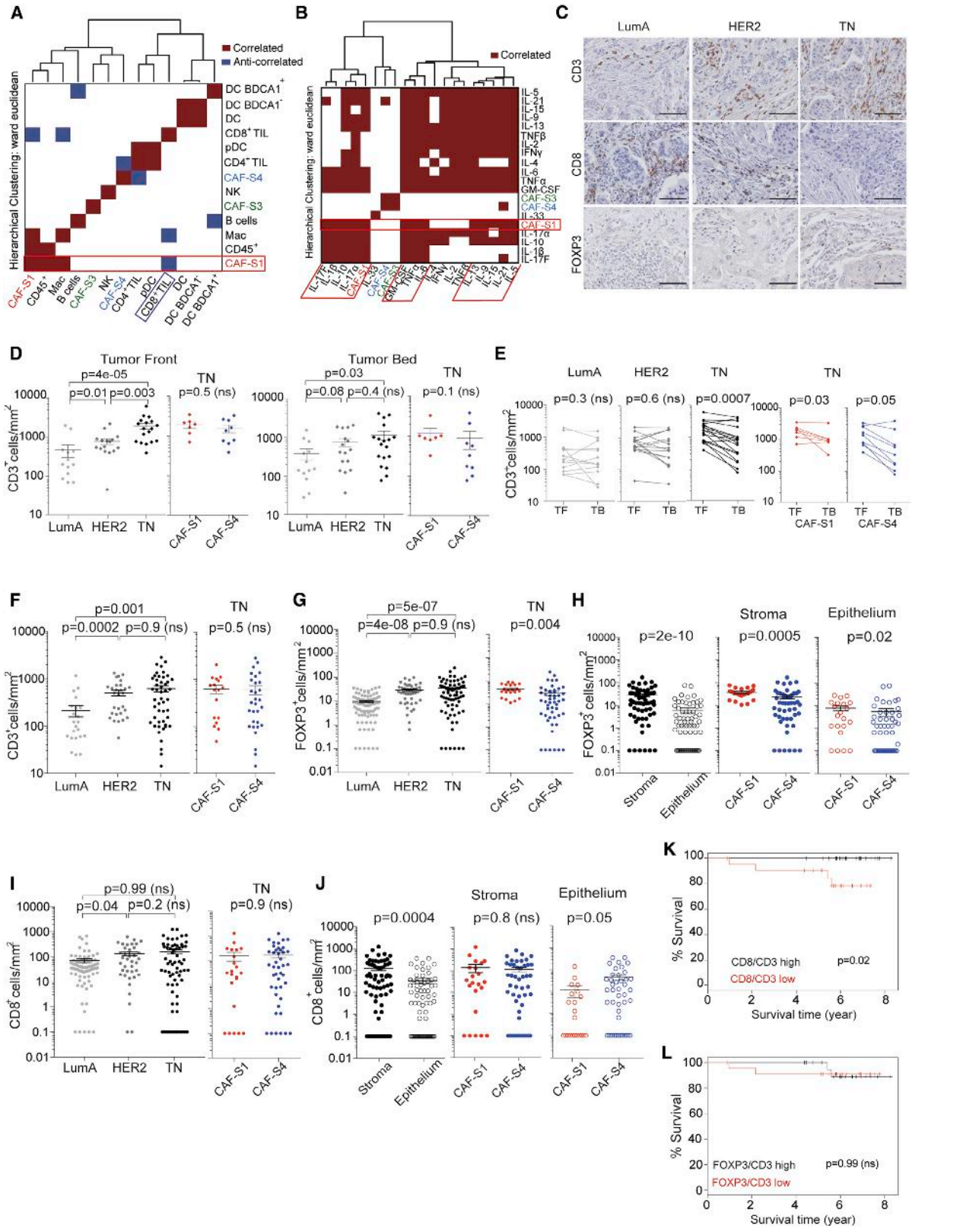

(legend on next page)

CAF-S1 Enrichment in BC Is Associated with Accumulation of FOXP3$^+$ T Lymphocytes

To investigate CAF subset biological functions, we analyzed the potential link between CAF subsets and immune infiltrates. To do so, fresh BC samples (Table S1; FACS prospective cohort) were characterized by FACS in terms of CAF subsets and infiltration by immune cells, including CD8$^+$ and CD4$^+$ T lymphocytes, macrophages, and dendritic and natural killer cells (Figure 3A). Interestingly, CAF-S1 fibroblasts were significantly correlated with CD45$^+$ hematopoietic cells and macrophages, but anti-correlated with CD8$^+$ T lymphocytes (Figure 3A). Anti-correlation between CAF-S1 and CD8$^+$ T cells was particularly high in TNBC patients (rho = −0.86; p = 0.02 by Spearman's test). In addition to CD45$^+$ hematopoietic cells, we found that the content of CAF-S1 fibroblasts was correlated with the infiltration of CD25$^+$ T lymphocytes (rho = 0.6; p = 0.02 by Spearman's test). We then screened the profiles of cytokines secreted from tumors and found that the CAF-S1 subset was significantly correlated with interleukins, such as interleukin-17F (IL-17F), IL-1β, IL-10, and IL-6 (Figure 3B).

To confirm the link between CAF-S1 and adaptive immunity in BC, we next analyzed CD3$^+$, CD8$^+$, and FOXP3$^+$ T lymphocytes by IHC (Figures 3C–3J). We first compared the content of CD3$^+$ T lymphocytes in tumor front (Figure S3A) and tumor bed (Figure 3C). Infiltration of CD3$^+$ T lymphocytes was higher in TNBC compared with LumA tumors both at tumor front and within tumor bed but without difference between CAF-S1- and CAF-S4-enriched TNBC (Figure 3D). In LumA and HER2 BC, the proportion of CD3$^+$ T lymphocytes was similar between tumor front and bed (Figure 3E). Of note, CD3$^+$ infiltration was significantly decreased in tumor bed compared with tumor front in TNBC, an effect detected both in CAF-S1- and CAF-S4-enriched TNBC (Figure 3E). Although tumor vascularization, assessed by staining of CD31$^+$ endothelial cells, was increased in TNBC compared with the other subtypes (Figure S3B), the increased infiltration of CD3$^+$ T lymphocytes remained higher in TNBC after normalization to the vessel content (Figure S3C). We validated that TNBC exhibited a higher proportion of CD3$^+$ T cells than LumA in an independent cohort of BC patients (Figure 3F). Moreover, FOXP3$^+$ T lymphocytes accumulated in TN compared with LumA tumors (Figure 3G). In addition, the stromal compartment of TNBC accumulated more FOXP3$^+$ T lymphocytes than the epithelium (Figure 3H). Interestingly, we observed an increase in the number of FOXP3$^+$ T cells in CAF-S1- compared with CAF-S4-enriched TNBC in stroma and epithelium, with a stronger effect in stroma (Figure 3H, middle and right). We next quantified the CD8$^+$ cytotoxic T lymphocytes in BC by IHC (Figures 3I and 3J). The CD8$^+$ infiltration in the tumor bed was lower in LumA than in HER2. In contrast, CD8$^+$ infiltration in TNBC displayed a bimodal distribution, with either high- or low-CD8$^+$ infiltration (Figures 3I and S3D). Moreover, we detected a significant reduction of CD8$^+$ T cell content in the epithelial compartment of CAF-S1-enriched TNBC compared with CAF-S4 tumors (Figure 3J). Although CAF-S1 or CAF-S4 contents did not exhibit any prognostic value on their own, TNBC patients with tumors highly infiltrated by CD8$^+$ or FOXP3$^+$ T lymphocytes (in stroma or epithelium) survived better than patients with low content (Figure S3E). This observation was consistent with the correlations observed between CD8$^+$ or FOXP3$^+$ T lymphocytes with CD3$^+$ T cells (Figure S3F) and suggest that better survival of TNBC patients is associated with a global high T cell infiltration, as previously reported (DeNardo et al., 2011; Liu et al., 2012; Ali et al., 2014). After normalization by the global content in CD3$^+$ cells, only CD8$^+$ T lymphocyte content remained indicative of good prognosis in TNBC, while FOXP3$^+$ T cell infiltration was not (Figures 3K and 3L). Thus, CAF-S1-enriched TNBC exhibit high infiltration of T lymphocytes with increased content in FOXP3$^+$ T cells, and concomitant reduction in CD8$^+$ T lymphocytes that might influence TNBC patient prognosis.

Molecular Characterization of CAF-S1 and CAF-S4 Subsets

We next characterized CAF-S1 transcriptomic profile and compared it with CAF-S4, the other activated CAF subset. We performed RNA sequencing from CAF-S1 and CAF-S4 fibroblasts sorted by FACS from human BC, using the same protocol as described above. Unsupervised analysis of the 500 most variable genes of CAF-S1 and CAF-S4 fibroblasts revealed that these two subsets exhibited distinct transcriptomic profiles (Figures 4A–4C). Indeed, PCA showed that the first component (explaining 40% of variance) was sufficient to explain the difference between CAF-S1 and CAF-S4 fibroblasts, while the second component (19% of variance) enabled us to distinguish samples from tumors and juxta-tumors (Figure 4A). Using the same PCA

Figure 3. Accumulation of CAF-S1 Fibroblasts Is Associated with Enrichment in FOXP3$^+$ T Lymphocytes

(A) Correlation matrix of CAF subsets and immune cells, quantified by FACS in BC (n = 12). Significant (p ≤ 0.05 by Pearson's test) correlations (red) and anti-correlations (blue) are shown.

(B) Correlation matrix between CAF subsets and cytokines quantified in BC supernatants (n = 36). Only significant correlations (red, p ≤ 0.05 by Pearson's test) are shown.

(C) Representative images of CD3$^+$, CD8$^+$, and FOXP3$^+$ T cells by IHC in tumor bed of LumA, HER2, and TNBC. Scale bars, 100 μm.

(D) Number of CD3$^+$ cells per mm^2 at tumor front (left) and bed (right) in LumA, HER2, and TNBC and in CAF-S1- or CAF-S4-enriched TNBC. Each dot represents one patient of the exploratory cohort (n = 60). Data are mean ± SEM. p values from Mann-Whitney test.

(E) Same as in (D) but analyzed by pair of tumor front (TF) and its corresponding tumor bed (TB) per BC sample. p values from Wilcoxon signed rank test.

(F) Number of CD3$^+$ per mm^2 in tumor bed of LumA, HER2, and TNBC (left) and in CAF-S1- or CAF-S4-enriched TNBC (right). Each dot represents one patient of the validation cohort (n = 272). Data are mean ± SEM. p values from Mann-Whitney test.

(G) Same as in (F) for FOXP3$^+$ T cells.

(H) Number of FOXP3$^+$ cells per mm^2 in stroma or epithelial compartments of TNBC (left), or in CAF-S1- and CAF-S4-enriched TNBC (middle, right). Each dot represents one TN patient of the validation cohort (n = 103). Data are mean ± SEM. p values from Mann-Whitney test.

(I) Same as in (F) for CD8$^+$ T cells.

(J) Same as in (H) for CD8$^+$ T cells.

(K and L) TNBC patient overall survival according to CD8$^+$/CD3$^+$ (K) or FOXP3$^+$/CD3$^+$ (L) ratio in tumor bed. TNBC patient subgroups with high (n = 23) or low (n = 22) CD8$^+$ or FOXP3$^+$ infiltration were defined using the median. p values based on log rank test. See also Figure S3 and Table S1.

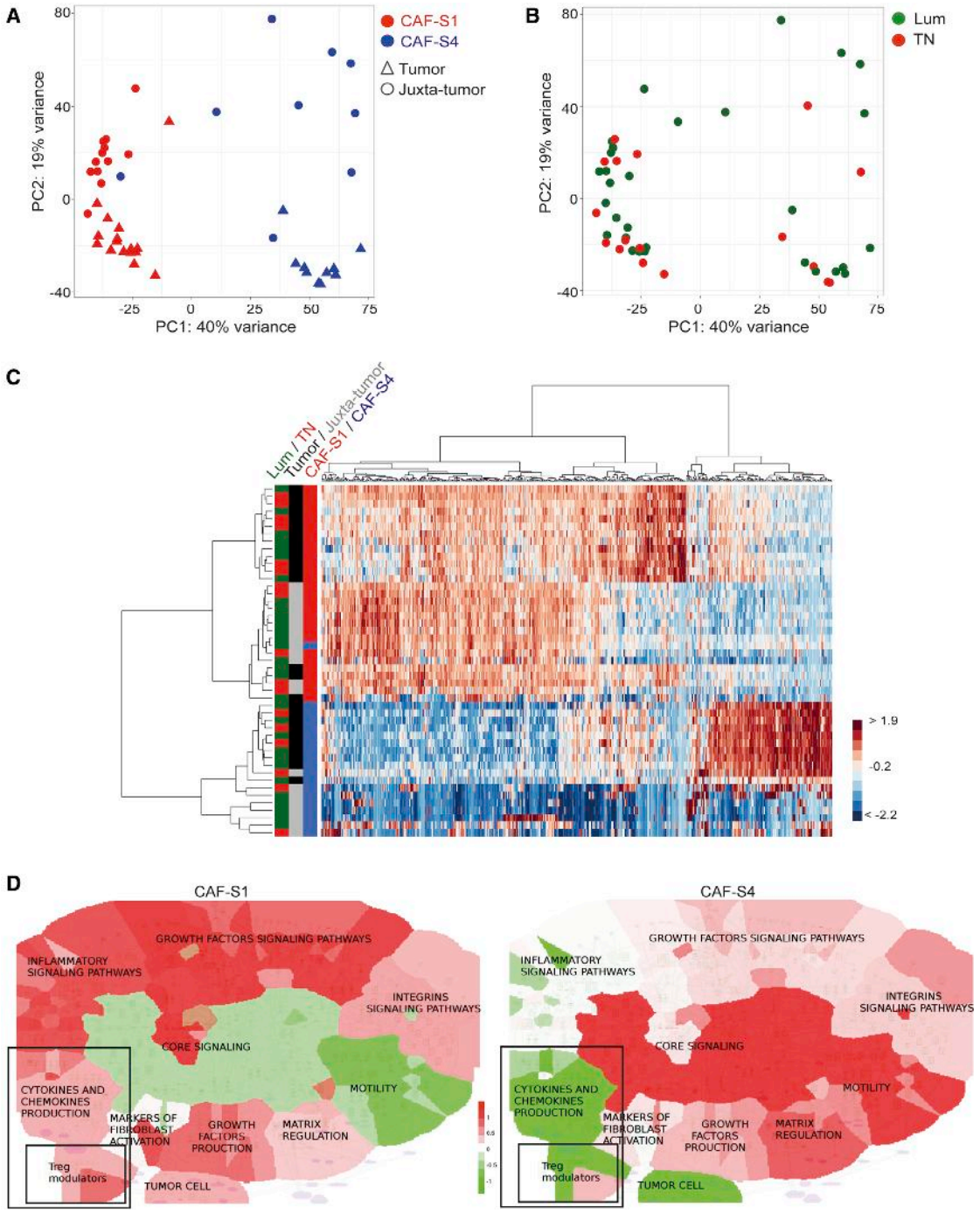

Figure 4. Molecular Characterization of CAF Subsets and Association of CAF-S1 with Immune Signaling Pathways

(A) PCA based on the 500 most variable genes from CAF-S1 and CAF-S4 RNA sequencing (RNA-seq) data. CAF-S1 (red, n = 28) and CAF-S4 (blue, n = 19) isolated from tumors (triangle, n = 26) or juxta-tumors (circle, n = 21).

(B) Same PCA representation as in (A), but each sample is colored according to BC subtype from which CAF-S1 or CAF-S4 were isolated (Lum, green; TN, red).

(C) Hierarchical clustering based on the 500 most variable genes from CAF-S1 and CAF-S4 RNA-seq data (n = 47). Clustering used Ward's method with Pearson distance. Rows represent CAF subset samples and columns the genes. The colors show the deviation of each gene expression from the mean, red and blue for values above and below the mean, respectively. Colors of the bars on the left of the heatmap indicate BC subtypes, tumor localization and CAF subsets.

(D) CAF molecular maps visualizing CAF-S1 (left) and CAF-S4 (right) transcriptomic profiles of a CAF-specific comprehensive map, manually curated from the literature and representing CAF molecular interactions in tumors. The map is divided into 11 functional modules. Upregulation of a functional module is in red, and downregulation in green. See also Figure S3, Tables S1, S3, S4, S5, and S6.

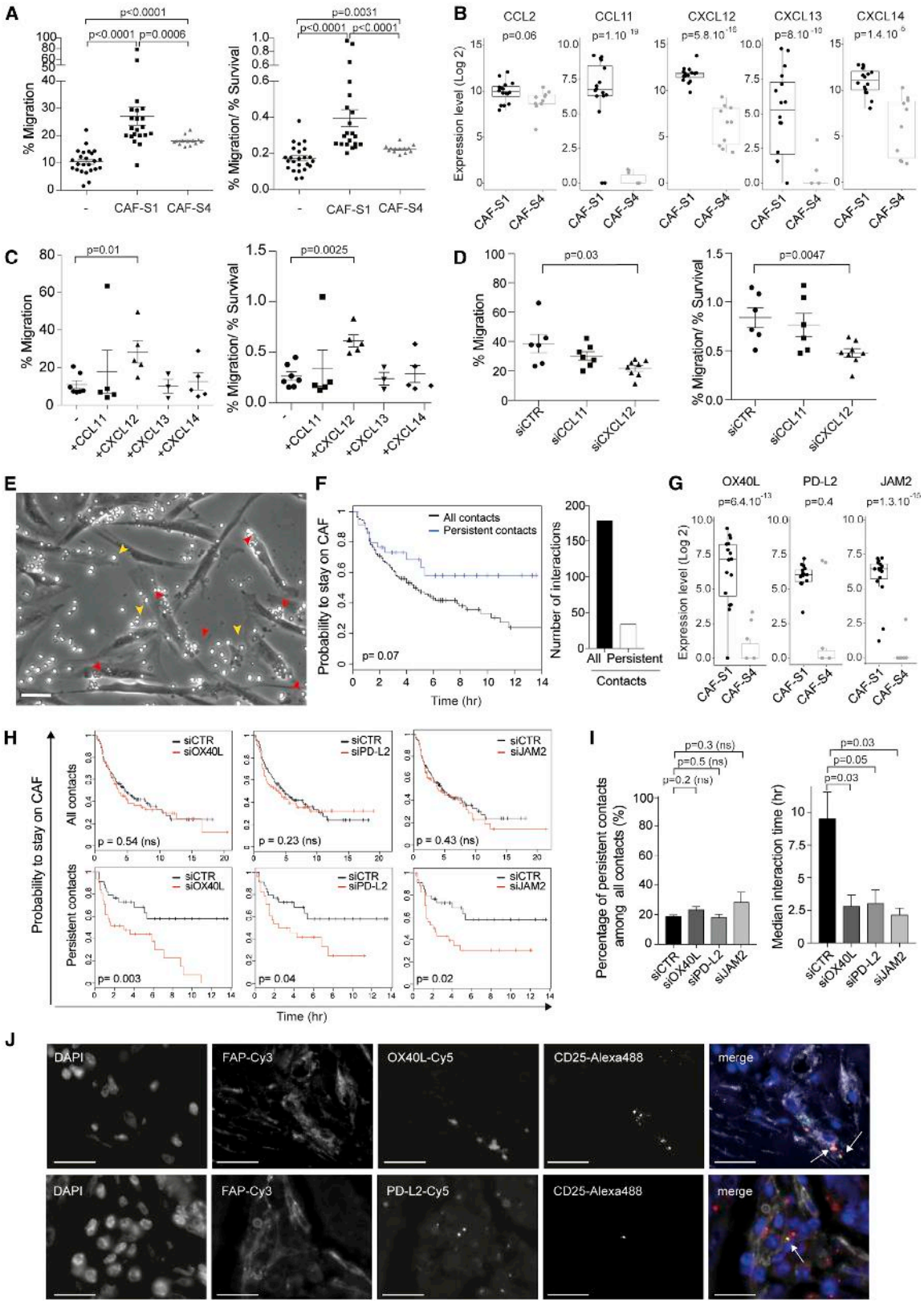

Figure 5. CAF-S1 Fibroblasts Promote Attraction and Retention of CD4$^+$CD25$^+$ T Cells

(A) Migration of CD4$^+$CD25$^+$ T cells (left) normalized by survival (right) in absence or presence of CAF-S1 or CAF-S4. Each dot represents an independent experiment ($n \geq 13$). Data are mean ± SEM. p values from Mann-Whitney (left) and Student's (middle and right) t tests.

(legend continued on next page)

representation established on CAF subsets, we next pointed out the distinct BC subtypes from which these CAF subpopulations were isolated (Figure 4B). CAF-S1 cells sorted from tumors (PC1 < 0; PC2 < 0; red triangles in Figure 4A) remained clustered, regardless of the BC subtype (green and red circles for Lum and TNBC, respectively, Figure 4B). Thus, a CAF-S1 isolated from Lum tumors exhibited similar identity as a CAF-S1 isolated from TNBC. The same conclusion could be drawn for CAF-S4. Hierarchical clustering confirmed that CAF-S1 and CAF-S4 subsets exhibited different transcriptomic profiles (Figure 4C). Thus, while their quantity differs in the different BC subtypes (with lower amount of both CAF-S1 and CAF-S4 in Lum compared with TNBC), CAF-S1 and CAF-S4 exhibit distinct identities. The biological interpretation of the differentially expressed genes based on gene ontology, Kyoto Encyclopedia of Genes and Genomes, and Ingenuity Pathway Analysis enabled us to define enriched relevant functions in CAF-S1 and CAF-S4 cells (Table S3). Genes upregulated in CAF-S1 subset were involved in cell adhesion, ECM organization, and immune response, while CAF-S4 fibroblasts were characterized by muscle contraction, regulation of actin cytoskeleton and oxidative metabolism. These pathways were similar considering either all BC subtypes or only TNBC (Table S3), thereby confirming that CAF-S1 and CAF-S4 identities are independent of BC subtypes. As CAF-S4 exhibited signatures close to pericytes, we validated using a specific pericyte marker (MCAM/CD146) that was able to detect MCAM-positive fibroblasts in BC (Figure S3G). Finally, tumors were enriched in cell adhesion and immune response pathways, while juxta-tumors were characterized by oxidative stress and lipid metabolic process (Tables S3 and S4). To better characterize the molecular functions of CAF subsets, a comprehensive map of molecular interactions was constructed using curation of the scientific literature. The map was further used for visualizing the transcriptomic profiles of CAF-S1 and CAF-S4 cells (Figure 4D; Table S5). This enabled us to confirm that, in comparison with CAF-S4, CAF-S1 exhibited a strong enrichment in immune signatures, including cytokines production and modulation of regulatory T lymphocytes (Tregs) (Figure 4D, left). Based on these observations, we identified key players highly expressed by CAF-S1 fibroblasts that could contribute to CAF-S1-mediated immunosuppression. To do so, we isolated a specific gene signature of CAF-S1 (Table S6) and determined a list of CAF-S1 upregulated genes known to be involved in immunomodulation (Zhang, 2010; Bindea et al., 2013; Segura et al., 2013; Barreira da Silva et al., 2015; Ramilowski et al., 2015). These genes belong to different biological processes, including chemokine signaling (CCL11, CXCL12, CXCL13, and CXCL14), cell adhesion (JAM2) or immunoregulatory functions (TNFSF4/OX40L, PDCD1LG2/PD-L2, DPP4, NT5E/CD73, and CD276/B7H3) that we further investigated in functional assays.

CAF-S1 Fibroblasts Promote Attraction and Retention of $CD4^+CD25^+$ T Lymphocytes

As CAF-S1-enriched stroma contains high number of $FOXP3^+$ T cells, we investigated the crosstalk between CAF-S1 and T lymphocytes. We hypothesized that CAF-S1 fibroblasts might act at different levels by promoting attraction of $CD4^+CD25^+$ T lymphocytes, favoring their retention, increasing their survival, and/or enhancing their differentiation into $CD25^{High}$ $FOXP3^{High}$ Tregs, all hypotheses being non-mutually exclusive. We performed *in vitro* functional assays comparing the properties of CAF-S1 and CAF-S4 subsets that mostly accumulate in TNBC. We isolated primary CAF-S1 and CAF-S4 fibroblasts from human BC and verified their identity (Figure S4A). We also isolated $CD4^+CD25^+$ T lymphocytes from peripheral blood mononuclear cells of healthy donors (Figure S4B). Using transwell assays, we first observed that CAF-S1, and, to a lesser extent CAF-S4, fibroblasts increased migration of $CD4^+CD25^+$ T lymphocytes, effect maintained when normalized for cell survival (Figure 5A). Chemokines, such as CCL2, expressed at similar levels in CAF-S1 and CAF-S4 (Figure 5B) might participate in T cell attraction, but could not explain the higher attractive capacity of CAF-S1 compared with CAF-S4 cells. Among the secreted molecules differentially expressed by CAF-S1 and CAF-S4 cells (such as CCL11, CXCL12, CXCL13, and CXCL14) (Figure 5B), exogenously added CXCL12 was the only chemokine able to increase T lymphocyte migration (Figure 5C). Accordingly, CXCL12 silencing in CAF-S1 fibroblasts (Figure S4C) strongly reduced T cell attraction to control levels (similar to that observed without CAFs) (Figure 5D, left), an effect independent of survival (Figure 5D, right). Despite its very high expression in CAF-S1 cells, CCL11 inactivation had no impact neither on T cell migration nor on survival (Figure 5D). To investigate the dynamic interaction between CAF-S1 fibroblasts and $CD4^+CD25^+$ T lymphocytes, we next performed time-lapse video-microscopy during 48 hr of co-culture of the two cell types (Figures 5E–5I). We first detected a close proximity between CAF-S1 cells and $CD4^+CD25^+$ T lymphocytes

(B) mRNA levels of CCL2, CCL11, CXCL12, CXCL13, and CXCL14 in CAF-S1 and CAF-S4 (n = 16 CAF-S1; n = 10 CAF-S4). Boxplots are shown as median ±25%–75% quantiles. p values from DESeq2.

(C) Migration of $CD4^+CD25^+$ T cells (left) normalized by survival (right) without or with CCL11, CXCL12, CXCL13, or CXCL14. Each dot represents an independent experiment ($n \geq 3$). Data are mean ± SEM. p values from Mann-Whitney (left) and Student's (right) t tests.

(D) Migration of $CD4^+CD25^+$ T cells (left) normalized by survival (right) in presence of CAF-S1 transfected with siCTR or siRNA against CCL11 or CXCL12. Each dot represents an independent experiment ($n \geq 6$). Data are mean ± SEM. p values from Mann-Whitney (left) and Student's (right) t tests.

(E) Microphotograph of CAF-S1 co-cultured with $CD4^+CD25^+$ T cells (Movie S1). Short-time contacts (yellow); persistent contacts (red arrows). Scale bars, 20 μm.

(F) Left: probability of $CD4^+CD25^+$ T cell to stay at the surface of CAF-S1 over time (hr). Each event is a loss of contact between T cells and CAF-S1. Either all (short and persistent) (black) or only persistent (blue) contacts in a representative experiment are shown. p value from log rank test. Right: number of contacts between CAF-S1 and $CD4^+CD25^+$ T cells.

(G) mRNA levels of OX40L, PD-L2, and JAM2 in CAF-S1 and CAF-S4, as in (B).

(H) Probability for a $CD4^+CD25^+$ T cell to stay at the surface of CAF-S1 transfected with siCTR (black) or with siRNA against OX40L, PD-L2, or siJAM2 (red). All (top) or persistent contacts (bottom) are considered. p values from log rank test.

(I) Percentage of persistent contacts among all contacts (left) and median interaction time of persistent contacts (right) of $CD4^+CD25^+$ T cells with CAF-S1 transfected with siCTR, siOX40L, siPD-L2, or siJAM2. Data are mean ± SEM. p values from Student's t test.

(J) Triple immunofluorescence showing co-staining (merged in yellow, white arrows) of $CD25^+$ (green), FAP (gray) and OX40L (red), or PD-L2 (red) on BC sections. Scale bars, 25 μm. See also Figure S4.

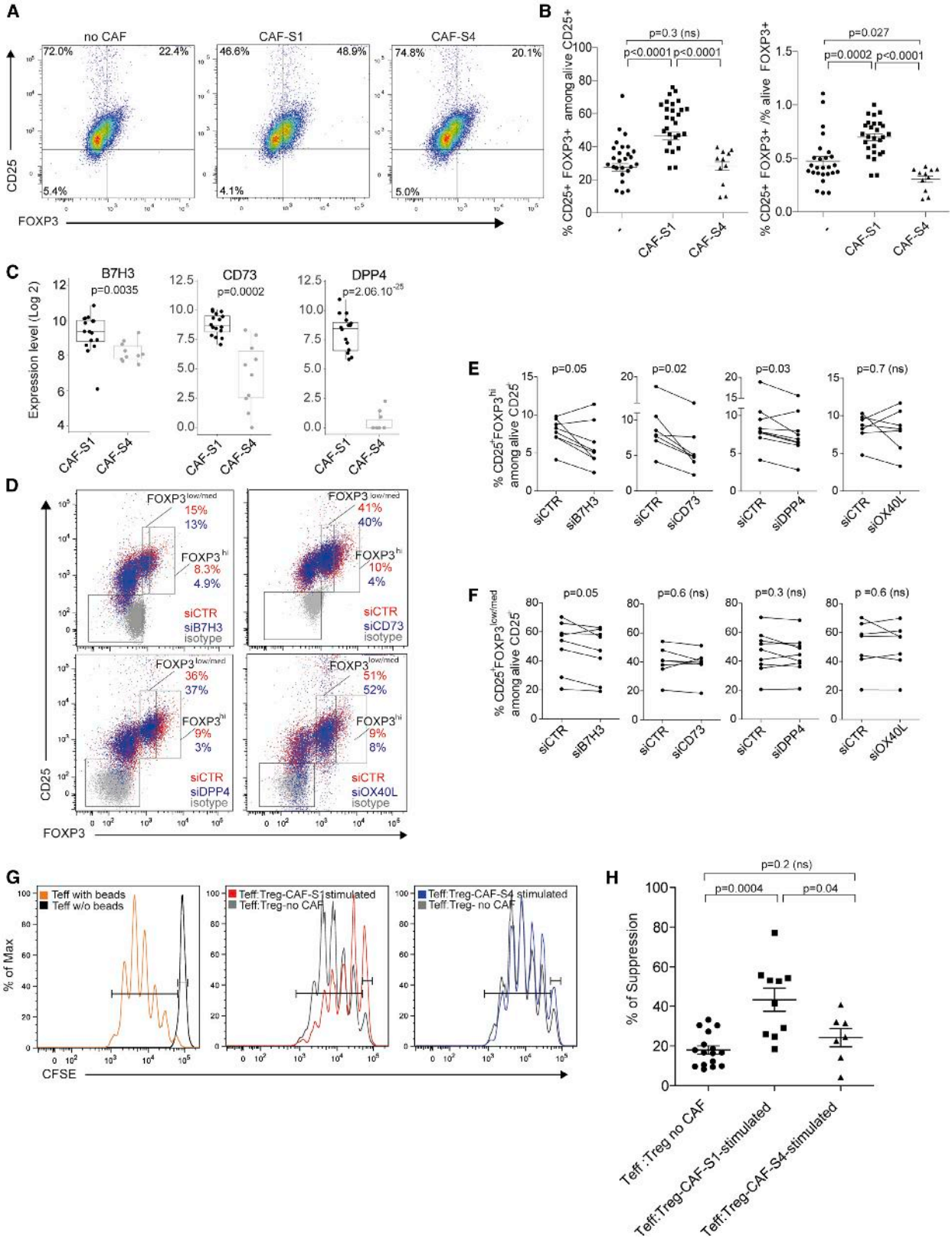

(legend on next page)

(Figure 5E), confirming the capacity of CAF-S1 cells to attract T cells. In addition, we observed two types of interaction between CAF-S1 fibroblasts and T cells: a short time contact (''come and go'') occurring during a short period of time (Figure 5E, yellow arrows) and a persistent interaction of at least 2 hr (Figure 5E, red arrows; Movie S1). We developed an automated tool to define the co-localization of CAF-S1 and immune cells and determine cell trajectories over time. We analyzed the interactions between immune and CAF-S1 cells over time and expressed it using Kaplan-Meier curves, where each event represented a loss of contact between the two cell types (Figure 5F). We found that the minimum median time of persistent interactions between CAF-S1 fibroblasts and $CD4^+CD25^+$ T lymphocytes exceeded 14 hr (Figure 5F, left). Moreover, the frequency of persistent interactions between CAF-S1 and T cells accounted for 20% of total contacts (Figure 5F, right). Among the genes highly expressed by CAF-S1 fibroblasts, we identified the ligands TNFSF4/OX40L and PDCD1LG2/PD-L2, as well as the adhesion molecule JAM2 (Figure 5G), as key players in long-term interactions between stromal and immune cells. Indeed, the median time of interaction dropped significantly (Figures 5H and 5I) upon silencing of these molecules in CAF-S1 cells (Figure S4D). Consistent with this, OX40 protein was detected at the surface of $CD4^+CD25^+$ T lymphocytes analyzed (Figure S4E). The frequency of persistent contacts between CAF-S1 and T cells (roughly 20% of total contacts) remained equivalent in all conditions (Figure 5I, left). However, the duration of retention of T lymphocytes was shortened by the silencing of OX40L, PD-L2, or JAM2 in CAF-S1 fibroblasts (Figure 5I, right), thus indicating that CAF-S1 retain $CD4^+CD25^+$ T cells at their surface through at least OX40L, PD-L2, and JAM2. PD-L2 and OX40L staining on human BC sections co-localized with $CD25^+$ T lymphocytes at the surface of CAF-S1-enriched stroma (Figure 5J), thereby confirming the relevance of these findings *in vivo*. Thus, CAF-S1 fibroblasts promote T lymphocyte attraction and retention at their surface through distinct mechanisms.

CAF-S1 Fibroblasts Enhance Regulatory T Cell Differentiation and Activity, while CAF-S4 Do Not Exhibit these Properties

We next tested the impact of CAF-S1 and CAF-S4 fibroblasts on the differentiation and activation of $CD25^+FOXP3^+$ T lymphocytes. CAF-S1 increased the total number of $CD25^+FOXP3^+$ T cells among the $CD25^+$ population (Figures 6A and 6B, left), an effect independent of survival (Figure 6B, right). In contrast, CAF-S4 had no effect (Figures 6A and 6B). We found that CD276/B7H3, NT5E/CD73, and DPP4 were highly expressed in CAF-S1, but not in CAF-S4 fibroblasts (Figure 6C). The silencing of CD276/B7H3, NT5E/CD73, or DPP4 in CAF-S1 fibroblasts (Figure S4F) significantly reduced the impact of CAF-S1 fibroblasts on the total number of $CD25^+FOXP3^+$ T cells, while inactivation of OX40L had no impact (Figures 6D–6F). Moreover, the impact of CD73 and DPP4 on $CD25^+FOXP3^+$ T cells activation was strictly observed in the $FOXP3^{high}$ population, while B7H3 had a broader effect by acting on both $FOXP3^{med}$ and $FOXP3^{high}$ populations (Figures 6E and 6F). Finally, we investigated the capacity of CAF-S1 and CAF-S4 cells to enhance Treg activity (Figures 6G and 6H). We found that the pre-culture of $CD25^{High}CD127^{low}CD45RA^{low}$ T lymphocytes with CAF-S1 fibroblasts significantly enhanced their capacity to inhibit effector T cell ($CD4^+CD25^-$) proliferation rate. In contrast, CAF-S4 cells were unable to display similar activity (Figures 6G and 6H). Taken as a whole, these observations show that CAF-S1 fibroblasts not only increase the content of $CD25^+FOXP3^+$ T cells, but also enhance their capacity to inhibit proliferation of effector T cells. In contrast, CAF-S4 fibroblasts are devoid of these activities.

DISCUSSION

Here, we discover the existence of four different CAF subsets in human BC that accumulate differently in BC subtypes and in normal juxta-tumors. Moreover, we identify the CAF-S1 fibroblast subset as a key player in immunosuppression. CAF-S1 fibroblasts attract T lymphocytes, increase the survival of $CD4^+CD25^+$ T lymphocytes, and promote their differentiation into $CD25^+FOXP3^+$ cells. CAF-S1 also enhances the capacity of Tregs to inhibit the proliferation of effector T cells. Importantly, CAF-S4 fibroblasts, the other myofibroblast subset identified, are devoid of this activity. Our work thus provides a multi-step mechanism by which a subset of myofibroblasts, here called CAF-S1, constitutes an immunosuppressive environment in BC (Figures 7A–7C).

Although CAFs are the most prominent stromal components, characterizing their heterogeneity in human cancers is far from

Figure 6. CAF-S1 Fibroblasts Enhance Regulatory T Cell Differentiation and Activity, while CAF-S4 Are Devoid of these Properties

(A) Representative FACS plots showing $CD25^+$ and $FOXP3^{+/-}$ cells without or with CAF-S1 or CAF-S4.

(B) Percentage of $CD25^+FOXP3^+$ (left) normalized to survival (right) without or with CAF-S1 or CAF-S4. Each dot represents an independent experiment ($n \geq 11$). Data are mean ± SEM. p values from Student's t test.

(C) mRNA levels of B7H3, CD73, and DPP4 in CAF-S1 and CAF-S4 (n = 16 CAF-S1; n = 10 CAF-S4). Boxplots are shown as median ±25%–75% quantiles. p values from DESeq2.

(D) Representative FACS plots showing $CD25^+$ and $FOXP3^{+/-}$ cells, upon co-culture with CAF-S1 transfected with siCTR (red) or siRNA against B7H3, CD73, DPP4, or OX40L (blue). Isotype control in gray. Gating of $CD25^+FOXP3^+$ was divided into $FOXP3^{low/med}$ or $FOXP3^{high}$. Percentages of T cells in each gate are indicated in red for siCTR and blue for siB7H3, siCD73, siDPP4, and siOX40L.

(E and F) $CD25^+FOXP3^{High}$ quantification upon co-culture with CAF-S1 transfected with siCTR or siRNA against siB7H3, siCD73, siDPP4, or siOX40L. Each dot represents an independent experiment ($n \geq 6$). p values from paired t test (siB7H3, siOX40L) or Wilcoxon signed-rank test (siCD73, siDPP4). (F) Same as in (E) for $CD25^+FOXP3^{Low/Med}$ T cells ($n \geq 6$). p values from Student's paired t test (siCD73, siDPP4, siOX40L) or Wilcoxon signed-rank test (siB7H3).

(G) Representative CFSE fluorescence intensity to assess $CD4^+$ effector T cell (Teff) proliferation. (left) Teff incubated without (black) or with CD3/CD28 beads (orange, ''Teff alone''); (middle, right) Teff incubated with CD3/CD28 beads, in presence of Treg ($CD4^+$ $CD25^{High}$ $CD127^{low}$ $CD45RA^{low}$) (Treg:Teff ratio of 2:1) pre-incubated overenight with CAF-S1 (red, middle) or CAF-S4 fibroblasts (blue, right) or in control medium (gray, middle and right).

(H) Quantification of the percentage of suppression calculated as follows: ((log2(y) of Teff alone – log2(y) of Teff + Treg)/log2(y) of Teff alone) × 100, where y is the MFI of CFSE on the whole population divided by the MFI of CFSE of non-proliferating cells. See also Figure S4.

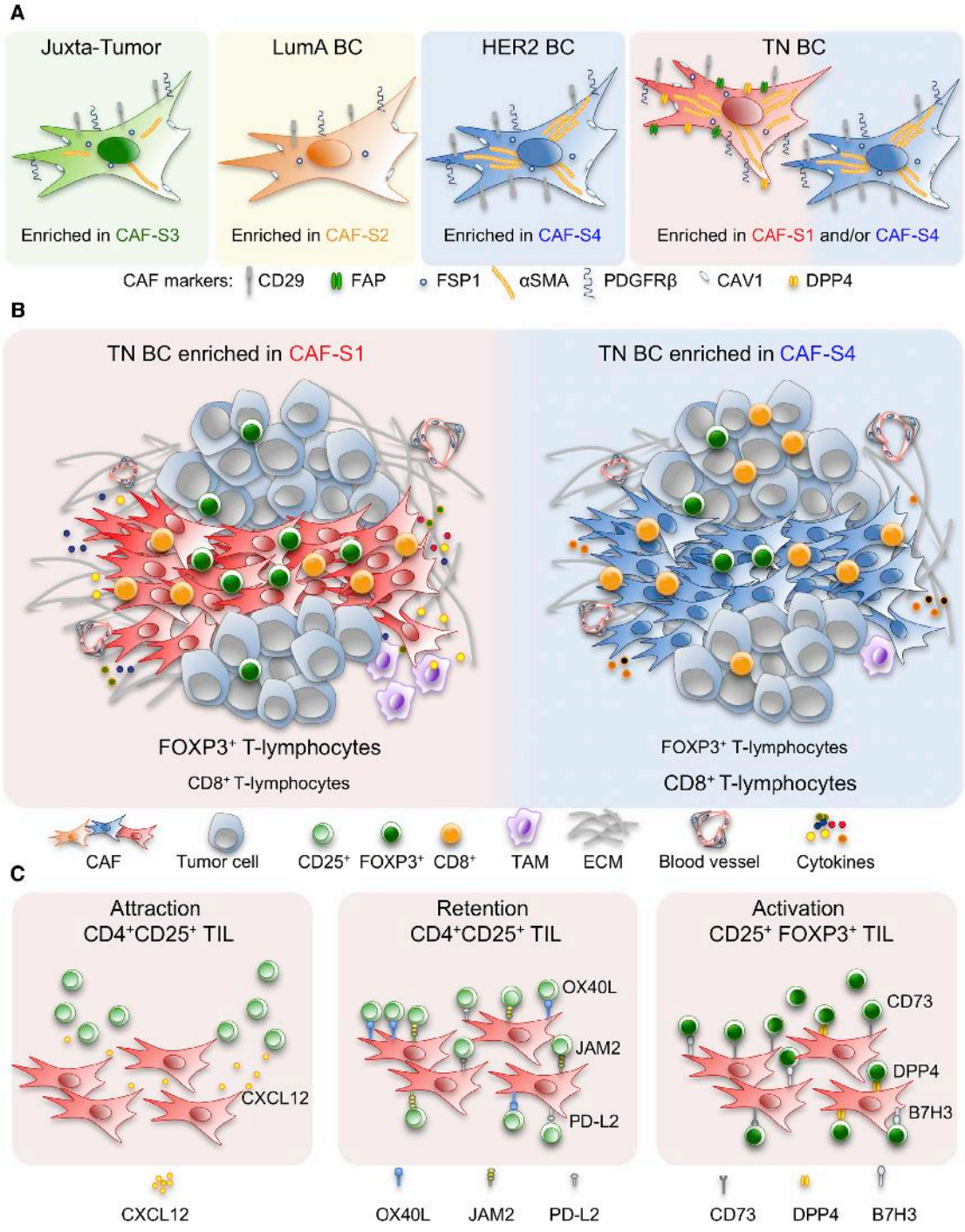

Figure 7. Schematic Representation of CAF Heterogeneity and T Lymphocyte Content in BC

(A) CAF heterogeneity in BC was addressed by analyzing six CAF markers (CD29, FSP1, FAP, αSMA, PDGFRβ, and CAV1) concomitantly. We identify four CAF subsets (CAF-S1 to CAF-S4) that accumulate differently in juxta-tumors compared with tumors and in BC subtypes. TNBC could be divided in two subgroups according to their enrichment in either CAF-S1 or CAF-S4.

(B) CAF-S1-enriched TNBC exhibit high content in FOXP3$^+$ T cells and low infiltration of CD8$^+$ T cells compared with CAF-S4-enriched tumors.

(C) CAF-S1 is associated with an immunosuppressive environment by acting at complementary levels: CAF-S1 attract CD4$^+$CD25$^+$ T cells mainly through the release of CXCL12, retain them through OX40L, PD-L2, and JAM2, promote their survival and stimulate their differentiation into CD25^{High}FOXP3^{High}, enriched in regulatory T cells, through B7H3, CD73, and DPP4. Finally, CAF-S1 enhance Treg-mediated inhibition of T effector proliferation, in contrast to CAF-S4. In summary, we demonstrate that half of TNBC accumulate a specific CAF subset that promotes an immunosuppressive microenvironment.

complete. A study performed in mouse pancreatic and BCs analyzed αSMA, PDGFRβ, and FSP1 altogether (Sugimoto et al., 2006) and already highlighted a certain degree of CAF heterogeneity. Here, we analyze six CAF markers in an integrated manner that enabled us to prove the existence of at least four CAF subsets in human BC. Both CAF-S1 ($CD29^{Med}$ FAP^{Hi} $FSP1^{Med}$ αSMA^{Hi} $PDGFR\beta^{Med\text{-}Hi}$ $CAV1^{Low}$) and CAF-S4 ($CD29^{Hi}$ FAP^{Neg} $FSP1^{Low\text{-}Med}$ αSMA^{Hi} $PDGFR\beta^{Low\text{-}Med}$ $CAV1^{Low}$) subsets are preferentially detected in aggressive (HER2 and TN) BC subtypes, thereby confirming that stromal myofibroblasts are markers of poor prognosis in BC. Similarly, we found a significant association between CAF subsets and BC subtypes, with accumulation of less activated CAFs in Lum tumors and enrichment of CAF-S1 in TNBC. CAF-S4 was distributed in Lum, HER2, and TN, but most HER2 BC are enriched in CAF-S4 subset. Moreover, TNBC are not a homogeneous group, but can be subdivided into two subgroups, enriched in CAF-S1 or CAF-S4 subsets. However, the CAF subsets on their own were not indicative of BC patient survival. This is in agreement with a previous study showing that FAP expression in stroma was not associated with clinicopathological factors, despite correlation with $CD45^{+}$ content (Tchou et al., 2013). Still CAF-S1 cells are often detected at close proximity of tumor cells, suggesting a mutual benefit for both CAF-S1 and cancer cells, as it was also recently reported in pancreatic cancers (Ohlund et al., 2017). CAF-S3 cells significantly accumulate in juxta-tumors. CAF-S3 are negative for FAP and αSMA but positive for CD29, FSP1, and PDGFRβ (FAP^{Neg} αSMA^{Neg} $CD29^{Med}$ $FSP1^{Med\text{-}Hi}$ $PDGFR\beta^{Med}$ $CAV1^{Low}$). Consistently, αSMA^{Neg} $PDGFR\alpha^{Pos}$ fibroblasts have been identified in both normal and neoplastic skin (Sugimoto et al., 2006; Erez et al., 2010), suggesting that αSMA^{Neg} $PDGFR\alpha^{Pos}$ and CAF-S3 cells could share some features. Several gene expression signatures have been tested in the past to appreciate stromal composition (Chang et al., 2005; Finak et al., 2008; Ma et al., 2009; Planche et al., 2011; Desmedt et al., 2012; Frings et al., 2013; Guo et al., 2013). Our data complement those by providing specific signatures of both CAF-S1 and CAF-S4. These gene signatures provide specific markers for each CAF subset and could be used to evaluate their proportion in tumors of various origins.

It is now recognized that both tumor and stromal cells can constitute an immunosuppressive environment to evade immune surveillance (Pardoll, 2012; Fearon, 2014). While the mechanisms by which tumor cells escape immune surveillance are now better understood, the role of stroma in immunosuppression is not yet elucidated, despite the potential for targeting CAF therapeutically (Takai et al., 2016). FAP^{Pos} cells have been demonstrated to exert an immunosuppressive activity in pancreatic and BC mouse models (Kraman et al., 2010; Feig et al., 2013; Yang et al., 2016; Zhang and Ertl, 2016). Here, we confirm these observations in human BC and uncover the involved mechanisms. We identify DPP4, a FAP-dimerization partner, as a key actor in CAF-S1-mediated Treg activation. In addition, CXCL12 is the most efficient to attract $CD4^{+}CD25^{+}$ T cells. This corroborates previous observations showing that CXCR4 inhibitors induce T cell accumulation and synergize with anti-PD-L1 treatment in mouse models (Feig et al., 2013; Ohlund et al., 2017). Studies over the past decade have demonstrated that immunotherapies can be effective in some tumors (Sugamura et al., 2004; Jensen et al., 2010), but it remains unclear why they are not successful in certain patients. Poorly immunogenic tumors could be resistant to immunotherapies, as well as to the use of OX40 agonists (Linch et al., 2015). Although OX40/OX40L signaling increases memory CD4 T cells and acts on Treg homeostasis (Takeda et al., 2004), we demonstrate that OX40L also enhances $CD4^{+}CD25^{+}$ T cell retention at the surface of CAF-S1. We can thus speculate on the potential adverse outcome of the use of OX40 agonist in CAF-S1-enriched tumors. In addition to OX40L, the immune checkpoint PD-L2 is also involved in $CD4^{+}CD25^{+}$ T cell retention by CAF-S1 cells. PD-L2 and PD-L1 are ligands of PD-1, but most of the studies focus on PD-L1/PD-1 (Freeman et al., 2000; Latchman et al., 2001), thereby leaving unknown the role of PD-L2 in immunotherapy resistance (Topalian et al., 2016). Moreover, immunotherapies based on PD-L1 blockade may not prevent interaction of PD-L2 with PD-1, so CAF-S1 could be a source of resistance to immunotherapies mediated by PD-L2. Finally, we provide evidence that CAF-S1 fibroblasts activate Tregs through B7H3, CD73, and DPP4. Immunotherapies based on drugs against B7H3 or CD73 have been developed to induce anti-tumor immunity (Zhou et al., 2007; Arigami et al., 2010; Loos et al., 2010; Terp et al., 2013; Seaman et al., 2017). Our study suggests that therapy against B7H3 or CD73 could also target CAF-S1 cells and enhance anti-tumor immunity by inhibiting CAF-S1-mediated immunosuppression. DPP4 was shown to cleave CXCL10, a chemokine capable of attracting effector T cells (Barreira da Silva et al., 2015). Blockade of DPP4 with the anti-diabetic drug Sitagliptin proved to be a useful immunotherapeutic agent by increasing effector T cells and ultimately reducing tumor growth in mice (Karagiannis et al., 2014; Barreira da Silva et al., 2015). In agreement, our results indicate that administration of FDA-approved anti-DPP4 drugs could be effective by acting at different levels in tumors, such as CAF-S1-enriched TNBC. In conclusion, targeting CAF-S1 might thus be a promising therapeutic approach, in complement to conventional treatments and immunotherapies.

STAR★METHODS

Detailed methods are provided in the online version of this paper and include the following:

- KEY RESOURCES TABLE
- CONTACT FOR REAGENT AND RESOURCE SHARING
- EXPERIMENTAL MODEL AND SUBJECT DETAILS
  - Cohorts of Breast Cancer Patients
  - Isolation and Culture of Primary CAF
- METHOD DETAILS
  - Flow Cytometry and Cell Sorting
  - Correlation between CAF Subsets and Immune Cells in BC
  - Screening of Cytokines from Tumor Supernatants
  - Immunohistochemistry (IHC)
  - Triple-Immunofluorescence Staining on BC Sections
  - Design of a Decision Tree for CAF Subset Prediction
  - Sensitivity Analysis of the CAF Decision Tree
  - Visualization of CAF Subsets *In Situ* at Cellular Level
  - RNA Sequencing of CAF-S1 and CAF-S4 Sorted from BC

SUPPLEMENTAL INFORMATION

Supplemental Information includes four figures, six tables, and one movie and can be found with this article online at https://doi.org/10.1016/j.ccell.2018.01.011.

ACKNOWLEDGMENTS

We are grateful to Pr. D. Louvard for fruitful discussions, J. Waterfall for critical reading of the manuscript, and E. Romano for discussion about immune checkpoint inhibitors. We thank Maude Delost for her advice on functional assays using T lymphocytes, Renaud Leclere, Elise Martel, and A. Nicolas from the experimental pathology platform (IC) for help and advice in IHC. We thank S. Baulande from the NGS platform (IC) for RNA-seq and U. Czerwinska for helping in the final visualization of the molecular CAF map. The authors acknowledge the Cell and Tissue Imaging (PICT-IBiSA) and the Nikon Imaging Center, Institut Curie, member of the French National Research Infrastructure France-BioImaging (ANR10-INBS-04). A.C. was supported by funding from the Fondation de France (2012-00034102) and the Fondation Pierre-Gilles de Gennes (FPGG0048). Y.K. was supported by the Institut National Du Cancer (INCa-DGOS-9963) and the Fondation pour la Recherche Médicale (FRM ING20130526797). M.C. was supported by the SiRIC-Curie program (INCa-DGOS-4654). The experimental work was supported by grants from the Institut National de la Santé et de la Recherche Médicale (Inserm), the Institut Curie, in particular the PIC TME and the PIC3i CAFi, the Ligue Nationale Contre le Cancer (Labelisation), the ICGex (ANR-10-EQPX-03), and INCa (INCa-DGOS-9963). We are very grateful to our funders for providing support these last years.

AUTHOR CONTRIBUTIONS

Conceptualization, F.M.-G; Methodology, F.M.-G., A.C., A.S.-D., and F.P.; Software, Y.K., C. Bernard, M.K., I.K., and A.Z.; Validation, F.M.-G., A.C., and Y.K.; Formal Analysis, Y.K. and A.Z.; Investigation, A.C., A.S.-D., F.P., B.B., M.C., P.S., I.M., A.-M.G., C. Bonneau, and M.-C.P.; Resources, A.V.-S., L.F., and V.S.; Data Curation, Y.K., M.K., I.K., and A.Z.; Writing – Original Draft, F.M.-G., A.C., and Y.K.; Writing – Review & Editing, F.M.-G., A.C., and Y.K.; Visualization, F.M.-G., A.C., and Y.K.; Supervision, F.M.-G.; Project Administration, F.M.-G.; Funding Acquisition, F.M.-G.

DECLARATION OF INTERESTS

F.M.-G., A.C., Y.K., A.-M.G., and F.P. are named inventors of an application for a patent (application deposit: EP17306013; July 28, 2017) based on the immunosuppressive players expressed by CAF-S1 that we identify here.

Received: August 3, 2017
Revised: November 16, 2017
Accepted: January 18, 2018
Published: February 15, 2018

REFERENCES

Ali, H.R., Provenzano, E., Dawson, S.J., Blows, F.M., Liu, B., Shah, M., Earl, H.M., Poole, C.J., Hiller, L., Dunn, J.A., et al. (2014). Association between CD8+ T-cell infiltration and breast cancer survival in 12,439 patients. Ann. Oncol. *25*, 1536–1543.

Allinen, M., Beroukhim, R., Cai, L., Brennan, C., Lahti-Domenici, J., Huang, H., Porter, D., Hu, M., Chin, L., Richardson, A., et al. (2004). Molecular characterization of the tumor microenvironment in breast cancer. Cancer Cell *6*, 17–32.

Ariga, N., Sato, E., Ohuchi, N., Nagura, H., and Ohtani, H. (2001). Stromal expression of fibroblast activation protein/seprase, a cell membrane serine proteinase and gelatinase, is associated with longer survival in patients with invasive ductal carcinoma of breast. Int. J. Cancer *95*, 67–72.

Arigami, T., Narita, N., Mizuno, R., Nguyen, L., Ye, X., Chung, A., Giuliano, A.E., and Hoon, D.S. (2010). B7-h3 ligand expression by primary breast cancer and associated with regional nodal metastasis. Ann. Surg. *252*, 1044–1051.

Barreira da Silva, R., Laird, M.E., Yatim, N., Fiette, L., Ingersoll, M.A., and Albert, M.L. (2015). Dipeptidylpeptidase 4 inhibition enhances lymphocyte trafficking, improving both naturally occurring tumor immunity and immunotherapy. Nat. Immunol. *16*, 850–858.

Benyahia, Z., Dussault, N., Cayol, M., Sigaud, R., Berenguer-Daizé, C., Delfino, C., Tounsi, A., Garcia, S., Martin, P.M., Mabrouk, K., and Ouafik, L. (2017). Stromal fibroblasts present in breast carcinomas promote tumor growth and angiogenesis through adrenomedullin secretion. Oncotarget *8*, 15744–15762.

Bindea, G., Mlecnik, B., Tosolini, M., Kirilovsky, A., Waldner, M., Obenauf, A.C., Angell, H., Fredriksen, T., Lafontaine, L., Berger, A., et al. (2013). Spatiotemporal dynamics of intratumoral immune cells reveal the immune landscape in human cancer. Immunity *39*, 782–795.

Chang, H.Y., Nuyten, D.S., Sneddon, J.B., Hastie, T., Tibshirani, R., Sorlie, T., Dai, H., He, Y.D., van't Veer, L.J., Bartelink, H., et al. (2005). Robustness, scalability, and integration of a wound-response gene expression signature in predicting breast cancer survival. Proc. Natl. Acad. Sci. USA *102*, 3738–3743.

Costa, A., Scholer-Dahirel, A., and Mechta-Grigoriou, F. (2014). The role of reactive oxygen species and metabolism on cancer cells and their microenvironment. Semin. Cancer Biol. *25*, 23–32.

DeNardo, D.G., Brennan, D.J., Rexhepaj, E., Ruffell, B., Shiao, S.L., Madden, S.F., Gallagher, W.M., Wadhwani, N., Keil, S.D., Junaid, S.A., et al. (2011). Leukocyte complexity predicts breast cancer survival and functionally regulates response to chemotherapy. Cancer Discov. *1*, 54–67.

Denton, A.E., Roberts, E.W., Linterman, M.A., and Fearon, D.T. (2014). Fibroblastic reticular cells of the lymph node are required for retention of resting but not activated CD8+ T cells. Proc. Natl. Acad. Sci. USA *111*, 12139–12144.

Desmedt, C., Majjaj, S., Kheddoumi, N., Singhal, S.K., Haibe-Kains, B., El Ouriaghli, F., Chaboteaux, C., Michiels, S., Lallemand, F., Journe, F., et al. (2012). Characterization and clinical evaluation of CD10+ stroma cells in the breast cancer microenvironment. Clin. Cancer Res. *18*, 1004–1014.

Dotto, G.P., Weinberg, R.A., and Ariza, A. (1988). Malignant transformation of mouse primary keratinocytes by Harvey sarcoma virus and its modulation by surrounding normal cells. Proc. Natl. Acad. Sci. USA *85*, 6389–6393.

Erez, N., Truitt, M., Olson, P., Arron, S.T., and Hanahan, D. (2010). Cancer-associated fibroblasts are activated in incipient neoplasia to orchestrate tumor-promoting inflammation in an NF-kappaB-dependent manner. Cancer Cell *17*, 135–147.

Fearon, D.T. (2014). The carcinoma-associated fibroblast expressing fibroblast activation protein and escape from immune surveillance. Cancer Immunol. Res. *2*, 187–193.

Feig, C., Jones, J.O., Kraman, M., Wells, R.J., Deonarine, A., Chan, D.S., Connell, C.M., Roberts, E.W., Zhao, Q., Caballero, O.L., et al. (2013). Targeting CXCL12 from FAP-expressing carcinoma-associated fibroblasts synergizes with anti-PD-L1 immunotherapy in pancreatic cancer. Proc. Natl. Acad. Sci. USA *110*, 20212–20217.

Finak, G., Bertos, N., Pepin, F., Sadekova, S., Souleimanova, M., Zhao, H., Chen, H., Omeroglu, G., Meterissian, S., Omeroglu, A., et al. (2008). Stromal gene expression predicts clinical outcome in breast cancer. Nat. Med. *14*, 518–527.

Freeman, G.J., Long, A.J., Iwai, Y., Bourque, K., Chernova, T., Nishimura, H., Fitz, L.J., Malenkovich, N., Okazaki, T., Byrne, M.C., et al. (2000). Engagement of the PD-1 immunoinhibitory receptor by a novel B7 family member leads to negative regulation of lymphocyte activation. J. Exp. Med. *192*, 1027–1034.

Frings, O., Augsten, M., Tobin, N.P., Carlson, J., Paulsson, J., Pena, C., Olsson, E., Veerla, S., Bergh, J., Ostman, A., and Sonnhammer, E.L. (2013). Prognostic significance in breast cancer of a gene signature capturing stromal PDGF signaling. Am. J. Pathol. *182*, 2037–2047.

Gascard, P., and Tlsty, T.D. (2016). Carcinoma-associated fibroblasts: orchestrating the composition of malignancy. Genes Dev. *30*, 1002–1019.

Gentric, G., Mieulet, V., and Mechta-Grigoriou, F. (2016). Heterogeneity in cancer metabolism: new concepts in an old field. Antioxid. Redox Signal. *26*, 462–485.

Goetz, J.G., Minguet, S., Navarro-Lérida, I., Lazcano, J.J., Samaniego, R., Calvo, E., Tello, M., Osteso-Ibáñez, T., Pellinen, T., Echarri, A., et al. (2011). Biomechanical remodeling of the microenvironment by stromal caveolin-1 favors tumor invasion and metastasis. Cell *146*, 148–163.

Guo, X., Zhu, S.X., Brunner, A.L., van de Rijn, M., and West, R.B. (2013). Next generation sequencing-based expression profiling identifies signatures from benign stromal proliferations that define stromal components of breast cancer. Breast Cancer Res. *15*, R117.

Hammer, A.M., Sizemore, G.M., Shukla, V.C., Avendano, A., Sizemore, S.T., Chang, J.J., Kladney, R.D., Cuitino, M.C., Thies, K.A., Verfurth, Q., et al. (2017). Stromal PDGFR-alpha activation enhances matrix stiffness, impedes mammary ductal development, and accelerates tumor growth. Neoplasia *19*, 496–508.

Jensen, S.M., Maston, L.D., Gough, M.J., Ruby, C.E., Redmond, W.L., Crittenden, M., Li, Y., Puri, S., Poehlein, C.H., Morris, N., et al. (2010). Signaling through OX40 enhances antitumor immunity. Semin. Oncol. *37*, 524–532.

Kalluri, R., and Zeisberg, M. (2006). Fibroblasts in cancer. Nat. Rev. Cancer *6*, 392–401.

Karagiannis, T., Boura, P., and Tsapas, A. (2014). Safety of dipeptidyl peptidase 4 inhibitors: a perspective review. Ther. Adv. Drug Saf. *5*, 138–146.

Kraman, M., Bambrough, P.J., Arnold, J.N., Roberts, E.W., Magiera, L., Jones, J.O., Gopinathan, A., Tuveson, D.A., and Fearon, D.T. (2010). Suppression of antitumor immunity by stromal cells expressing fibroblast activation protein-alpha. Science *330*, 827–830.

Kuperstein, I., Bonnet, E., Nguyen, H.A., Cohen, D., Viara, E., Grieco, L., Fourquet, S., Calzone, L., Russo, C., Kondratova, M., et al. (2015). Atlas of cancer signalling network: a systems biology resource for integrative analysis of cancer data with google maps. Oncogenesis *4*, e160.

Latchman, Y., Wood, C.R., Chernova, T., Chaudhary, D., Borde, M., Chernova, I., Iwai, Y., Long, A.J., Brown, J.A., Nunes, R., et al. (2001). PD-L2 is a second ligand for PD-1 and inhibits T cell activation. Nat. Immunol. *2*, 261–268.

Lee, W.Y., Su, W.C., Lin, P.W., Guo, H.R., Chang, T.W., and Chen, H.H. (2004). Expression of S100A4 and Met: potential predictors for metastasis and survival in early-stage breast cancer. Oncology *66*, 429–438.

Linch, S.N., McNamara, M.J., and Redmond, W.L. (2015). OX40 agonists and combination immunotherapy: putting the pedal to the metal. Front. Oncol. *5*, 34.

Liu, S., Lachapelle, J., Leung, S., Gao, D., Foulkes, W.D., and Nielsen, T.O. (2012). CD8+ lymphocyte infiltration is an independent favorable prognostic indicator in basal-like breast cancer. Breast Cancer Res. *14*, R48.

Loos, M., Hedderich, D.M., Friess, H., and Kleeff, J. (2010). B7-h3 and its role in antitumor immunity. Clin. Dev. Immunol. *2010*, 683875.

Ma, X.J., Dahiya, S., Richardson, E., Erlander, M., and Sgroi, D.C. (2009). Gene expression profiling of the tumor microenvironment during breast cancer progression. Breast Cancer Res. *11*, R7.

Ohlund, D., Handly-Santana, A., Biffi, G., Elyada, E., Almeida, A.S., Ponz-Sarvise, M., Corbo, V., Oni, T.E., Hearn, S.A., Lee, E.J., et al. (2017). Distinct populations of inflammatory fibroblasts and myofibroblasts in pancreatic cancer. J. Exp. Med. *214*, 579–596.

Olumi, A.F., Grossfeld, G.D., Hayward, S.W., Carroll, P.R., Tlsty, T.D., and Cunha, G.R. (1999). Carcinoma-associated fibroblasts direct tumor progression of initiated human prostatic epithelium. Cancer Res. *59*, 5002–5011.

Orimo, A., Gupta, P.B., Sgroi, D.C., Arenzana-Seisdedos, F., Delaunay, T., Naeem, R., Carey, V.J., Richardson, A.L., and Weinberg, R.A. (2005). Stromal fibroblasts present in invasive human breast carcinomas promote tumor growth and angiogenesis through elevated SDF-1/CXCL12 secretion. Cell *121*, 335–348.

Ozdemir, B.C., Pentcheva-Hoang, T., Carstens, J.L., Zheng, X., Wu, C.C., Simpson, T.R., Laklai, H., Sugimoto, H., Kahlert, C., Novitskiy, S.V., et al. (2014). Depletion of carcinoma-associated fibroblasts and fibrosis induces immunosuppression and accelerates pancreas cancer with reduced survival. Cancer Cell *25*, 719–734.

Pardoll, D.M. (2012). The blockade of immune checkpoints in cancer immunotherapy. Nat. Rev. Cancer *12*, 252–264.

Paulsson, J., Ehnman, M., and Ostman, A. (2014). PDGF receptors in tumor biology: prognostic and predictive potential. Future Oncol. *10*, 1695–1708.

Paulsson, J., Ryden, L., Strell, C., Frings, O., Tobin, N.P., Fornander, T., Bergh, J., Landberg, G., Stal, O., and Ostman, A. (2017). High expression of stromal PDGFRbeta is associated with reduced benefit of tamoxifen in breast cancer. J. Pathol. Clin. Res. *3*, 38–43.

Perou, C.M., Sørlie, T., Eisen, M.B., van de Rijn, M., Jeffrey, S.S., Rees, C.A., Pollack, J.R., Ross, D.T., Johnsen, H., Akslen, L.A., et al. (2000). Molecular portraits of human breast tumours. Nature *406*, 747–752.

Planche, A., Bacac, M., Provero, P., Fusco, C., Delorenzi, M., Stehle, J.C., and Stamenkovic, I. (2011). Identification of prognostic molecular features in the reactive stroma of human breast and prostate cancer. PLoS One *6*, e18640.

Qiu, P., Simonds, E.F., Bendall, S.C., Gibbs, K.D., Jr., Bruggner, R.V., Linderman, M.D., Sachs, K., Nolan, G.P., and Plevritis, S.K. (2011). Extracting a cellular hierarchy from high-dimensional cytometry data with SPADE. Nat. Biotechnol. *29*, 886–891.

Ramilowski, J.A., Goldberg, T., Harshbarger, J., Kloppmann, E., Lizio, M., Satagopam, V.P., Itoh, M., Kawaji, H., Carninci, P., Rost, B., and Forrest, A.R. (2015). A draft network of ligand-receptor-mediated multicellular signalling in human. Nat. Commun. *6*, 7866.

Rudland, P.S., Platt-Higgins, A., Renshaw, C., West, C.R., Winstanley, J.H., Robertson, L., and Barraclough, R. (2000). Prognostic significance of the metastasis-inducing protein S100A4 (p9Ka) in human breast cancer. Cancer Res. *60*, 1595–1603.

Ruhland, M.K., Loza, A.J., Capietto, A.H., Luo, X., Knolhoff, B.L., Flanagan, K.C., Belt, B.A., Alspach, E., Leahy, K., Luo, J., et al. (2016). Stromal senescence establishes an immunosuppressive microenvironment that drives tumorigenesis. Nat. Commun. *7*, 11762.

Saltelli, A., Tarantola, S., Campolongo, F., and Ratto, M. (2004). Sensitivity Analysis in Practice: A Guide to Assessing Scientific Models (John Wiley & Sons, Ltd).

Seaman, S., Zhu, Z., Saha, S., Zhang, X.M., Yang, M.Y., Hilton, M.B., Morris, K., Szot, C., Morris, H., Swing, D.A., et al. (2017). Eradication of tumors through simultaneous ablation of CD276/B7-H3-positive tumor cells and tumor vasculature. Cancer Cell *31*, 501–515.e508.

Segura, E., Touzot, M., Bohineust, A., Cappuccio, A., Chiocchia, G., Hosmalin, A., Dalod, M., Soumelis, V., and Amigorena, S. (2013). Human inflammatory dendritic cells induce Th17 cell differentiation. Immunity *38*, 336–348.

Simpkins, S.A., Hanby, A.M., Holliday, D.L., and Speirs, V. (2012). Clinical and functional significance of loss of caveolin-1 expression in breast cancer-associated fibroblasts. J. Pathol. *227*, 490–498.

Sorlie, T., Perou, C.M., Tibshirani, R., Aas, T., Geisler, S., Johnsen, H., Hastie, T., Eisen, M.B., van de Rijn, M., Jeffrey, S.S., et al. (2001). Gene expression patterns of breast carcinomas distinguish tumor subclasses with clinical implications. Proc. Natl. Acad. Sci. USA *98*, 10869–10874.

Straussman, R., Morikawa, T., Shee, K., Barzily-Rokni, M., Qian, Z.R., Du, J., Davis, A., Mongare, M.M., Gould, J., Frederick, D.T., et al. (2012). Tumour micro-environment elicits innate resistance to RAF inhibitors through HGF secretion. Nature *487*, 500–504.

Sugamura, K., Ishii, N., and Weinberg, A.D. (2004). Therapeutic targeting of the effector T-cell co-stimulatory molecule OX40. Nat. Rev. Immunol. *4*, 420–431.

Sugimoto, H., Mundel, T.M., Kieran, M.W., and Kalluri, R. (2006). Identification of fibroblast heterogeneity in the tumor microenvironment. Cancer Biol. Ther. *5*, 1640–1646.

Takai, K., Le, A., Weaver, V.M., and Werb, Z. (2016). Targeting the cancer-associated fibroblasts as a treatment in triple-negative breast cancer. Oncotarget *7*, 82889–82901.

Takeda, I., Ine, S., Killeen, N., Ndhlovu, L.C., Murata, K., Satomi, S., Sugamura, K., and Ishii, N. (2004). Distinct roles for the OX40-OX40 ligand interaction in regulatory and nonregulatory T cells. J. Immunol. *172*, 3580–3589.

Tan, W., Zhang, W., Strasner, A., Grivennikov, S., Cheng, J.Q., Hoffman, R.M., and Karin, M. (2011). Tumour-infiltrating regulatory T cells stimulate mammary cancer metastasis through RANKL-RANK signalling. Nature *470*, 548–553.

Tchou, J., Zhang, P.J., Bi, Y., Satija, C., Marjumdar, R., Stephen, T.L., Lo, A., Chen, H., Mies, C., June, C.H., et al. (2013). Fibroblast activation protein expression by stromal cells and tumor-associated macrophages in human breast cancer. Hum. Pathol. *44*, 2549–2557.

Terp, M.G., Olesen, K.A., Arnspang, E.C., Lund, R.R., Lagerholm, B.C., Ditzel, H.J., and Leth-Larsen, R. (2013). Anti-human CD73 monoclonal antibody inhibits metastasis formation in human breast cancer by inducing clustering and internalization of CD73 expressed on the surface of cancer cells. J. Immunol. *191*, 4165–4173.

Topalian, S.L., Taube, J.M., Anders, R.A., and Pardoll, D.M. (2016). Mechanism-driven biomarkers to guide immune checkpoint blockade in cancer therapy. Nat. Rev. Cancer *16*, 275–287.

Toullec, A., Gerald, D., Despouy, G., Bourachot, B., Cardon, M., Lefort, S., Richardson, M., Rigaill, G., Parrini, M.C., Lucchesi, C., et al. (2010). Oxidative stress promotes myofibroblast differentiation and tumour spreading. EMBO Mol. Med. *2*, 211–230.

Yang, X., Lin, Y., Shi, Y., Li, B., Liu, W., Yin, W., Dang, Y., Chu, Y., Fan, J., and He, R. (2016). FAP promotes immunosuppression by cancer-associated fibroblasts in the tumor microenvironment via STAT3-CCL2 signaling. Cancer Res. *76*, 4124–4135.

Zaragoza, B., Chen, X., Oppenheim, J.J., Baeyens, A., Gregoire, S., Chader, D., Gorochov, G., Miyara, M., and Salomon, B.L. (2016). Suppressive activity of human regulatory T cells is maintained in the presence of TNF. Nat. Med. *22*, 16–17.

Zhang, B. (2010). CD73: a novel target for cancer immunotherapy. Cancer Res. *70*, 6407–6411.

Zhang, Y., and Ertl, H.C. (2016). Depletion of FAP+ cells reduces immunosuppressive cells and improves metabolism and functions CD8+ T cells within tumors. Oncotarget *7*, 23282–23299.

Zhou, X., Zhi, X., Zhou, P., Chen, S., Zhao, F., Shao, Z., Ou, Z., and Yin, L. (2007). Effects of ecto-5'-nucleotidase on human breast cancer cell growth in vitro and in vivo. Oncol. Rep. *17*, 1341–1346.

STAR★METHODS

KEY RESOURCES TABLE

REAGENT or RESOURCE	SOURCE	IDENTIFIER
Antibodies		
anti-EpCAM-PerCR/Cy5.5	BioLegend	Cat#324214; RRID:AB_2098808
anti-CD31-PECy7	BioLegend	Cat#303118; RRID:AB_2247932
anti-CD45-APC-Cy7	BD Biosciences	Cat#BD-557833; RRID:AB_396891
anti-CD29-Alexa Fluor 700	BioLegend	Cat#303020; RRID:AB_2130078
anti-FAP used coupled with Pacific Orange	R&D Systems	Cat#MAB3715; RRID:AB_2102368
Pacific Orange	Thermo Fisher Scientific	Cat#Z25269
anti-PDGFRβ-PE	BioLegend	Cat#323606; RRID:AB_2268134
anti-Caveolin1-FITC	Santa Cruz	Cat#70516; RRID:AB_1120056
anti-SMA-APC	R&D Systems	Cat#IC1420A; RRID:AB_10890600
anti-S100A4 (FSP1) used coupled with Alexa Fluor 647-RPE	Abcam	Cat#ab27957; RRID:AB_2183775
Alexa Fluor 647-RPE	Thermo Fisher Scientific	Cat#A-20991; RRID:AB_2535705
Alexa Fluor 700 mouse IgG1 (Isotype anti-CD29)	BioLegend	Cat#400144
Mouse IgG1 isotype control (Isotype anti-FAP)	R&D Systems	Cat#MAB002; RRID:AB_357344
PE Mouse IgG1 (isotype anti-PDGFRβ)	BioLegend	Cat#400114
Mouse IgG2b FITC (isotype anti-CAV1)	Santa Cruz	Cat#2857; RRID:AB_737258
Mouse IgG2A APC (isotype anti-SMA)	R&D Systems	Cat#IC003A; RRID:AB_357243
Rabbit IgG (isotype anti-FSP1)	Abcam	Cat#ab27472
IgG negative control beads for FACS	BD biosciences	Cat#552843
ArC reactive beads	Molecular probes	Cat#A10346
anti-CD14	Invitrogen	Cat#Q10013; RRID:AB_2556439
Brilliant Violet 650 anti-CD11b	Biolegend	Cat#101239; RRID:AB_11125575
Brilliant Violet 711 anti-HLADR	Biolegend	Cat#307643; RRID:AB_11218794
Brilliant Violet 785 anti-CD19	Biolegend	Cat#302239; RRID:AB_11218596
anti-CD16	BD Biosciences	Cat#335035
anti-CD4	Miltenyi Biotec	Cat#130092374; RRID:AB_871680
anti-CD8	Invitrogen	Cat#MHCD0822; RRID:AB_10392700
anti-CD11c	BD Biosciences	Cat#551077; RRID:AB_394034
PE anti-CD1c (anti-BDCA1)	Biolegend	Cat#331506; RRID:AB_1088999
Anti-integrin beta 1 (anti-CD29)	Abcam	Cat#ab3167; RRID:AB_303570
anti-FAP	Abcam	Cat#ab53066; RRID:AB_880077
anti-FAP	Vitatex	Cat#MABS1001
anti-FSP1	Abcam	Cat#ab27472
anti-PDGFRβ	Abcam	Cat#ab32570; RRID:AB_777165
anti-SMA	Dako	Cat#M0851; RRID:AB_2223500
anti-CAV1	BD Biosciences	Cat#610060; RRID:AB_397472
anti-MCAM/CD146	Sigma	Cat#HPA008848; RRID:AB_1078445
anti-CD3	Dako	Cat#M7254; RRID:AB_2631163
anti-CD8	Dako	Cat#M4103
anti-FOXP3	Abcam	Cat#ab20034; RRID:AB_445284
anti-CD31	Dako	Cat#M0823; RRID:AB_2114471
anti-OX40L	Cell Signaling	Cat#59036
anti-PD-L2	Sigma	Cat#HPA013411; RRID:AB_1855102
anti-CD25	Invitrogen	Cat#MA5-12680; RRID:AB_10979943

(*Continued on next page*)

Continued

REAGENT or RESOURCE	SOURCE	IDENTIFIER
anti-EpCAM-BV605	BioLegend	Cat#324224; RRID:AB_2562518
anti-CD31-PECy7	BioLegend	Cat#303118; RRID:AB_2247932
anti-CD45-APC-Cy7	BD Biosciences	Cat#BD-557833; RRID:AB_396891
anti-CD29-Alexa Fluor 700	BioLegend	Cat#303020; RRID:AB_2130078
anti-FAP-APC	R&D Systems	Cat#MAB3715; RRID:AB_2102368
anti-PDGFRβ-BV405	BD Biosciences	Cat#BD-564124
anti-SMA-AlexaFluor594	R&D Systems	Cat#IC1420T
anti-FSP1-PE	BioLegend	Cat#370004; RRID:AB_2572072
anti-DPP4-BV650	BD Biosciences	Cat#744451
anti-CD25	BD Pharmigen	Cat#557741; RRID:AB_396847
anti-CD127	Thermo Fisher	Cat#11-1278-42; RRID:AB_1907342
anti-CD45RA	BD Pharmigen	Cat#555489; RRID:AB_395880
anti-Foxp3-Alexa Fluor 488	eBioscience	Cat#53-4776; RRID:AB_10801948
Anti-CD4-APC	Miltenyi Biotec	Cat# 130-092-374; RRID:AB_871680
anti-CD25-PE	Miltenyi Biotec	Cat#130-091-024; RRID:AB_244320
Mouse IgG2b PE (isotype anti-CD25)	Miltenyi Biotec	Cat#130-092-215; RRID:AB_871719
Rat IgG2a Alexa Fluor 488 (isotype anti-FOXP3)	eBioscience	Cat#53-4321; RRID:AB_493963
Biological Samples		
Breast fresh tumors	Institut Curie Hospital group	N/A
FFPE Breast sections	Institut Curie Hospital group	N/A
Chemicals, Peptides, and Recombinant Proteins		
collagenase I	Sigma-Aldrich	Cat#C0130
hyaluronidase	Sigma-Aldrich	Cat#H3506
DNase I	Roche	Cat#11284932001
Saponin	Sigma-Aldrich	Cat#S7900
Target retrieval solution citrate pH 6	Dako	Cat#S2369
Target retrieval solution citrate pH 9	Dako	Cat#S202386
3,3'-diaminobenzidine for 5 min (DAB)	Dako	Cat#K3468
EnVision FLEX Target Retrieval Solution high pH	Dako	Cat#K800421
EnVision FLEX Target Retrieval Solution low pH	Dako	Cat#K800521
EnVision FLEX/HRP	Dako	Cat#K8006
Vectashield with DAPI	Vector Laboratories	Cat#H-1200
Dako REAL peroxidase-blocking solution	Dako	Cat#S202386
DharmaFECT	Dharmacon	Cat#T-2001-02
Lymphoprep	STEMCELL	Cat#07861
carboxylated beads	Polyscience	Cat#18133
Human CCL11	Peprotech	Cat#300-21
Human CXCL12	Peprotech	Cat#300-28A
Human CXCL13	Peprotech	Cat#300-47
Human CXCL14	Peprotech	Cat#300-50
Dynabeads Hyman T-activator CD3/CD28 beads	Gibco	Cat#11131D
LIVE/DEAD dye	Thermo Fisher Scientific	Cat#L34955
LIVE/DEAD™ Fixable Aqua Dead Cell Stain dye	Thermo Fisher Scientific	Cat#L34957
Critical Commercial Assays		
Vectastain ABC kit mouse IgG	VECTOR laboratories	Cat#PK-6102
Vectastain ABC kit rabbit IgG	VECTOR laboratories	Cat#PK-6101
AlexaFluor 647 Tyramide SuperBoost Kit	Invitrogen	Cat#B40926
Single Cell Purification kit	Norgen Biotek	Cat#51800
SMARTer Ultra Low Input RNA kit	Clontech	Cat#634826

(*Continued on next page*)

Continued

REAGENT or RESOURCE	SOURCE	IDENTIFIER
Agilent RNA 6000 Pico kit	Agilent Technologies	Cat#5067-1513
Agilent High Sensitivity DNA kit	Agilent Technologies	Cat#5067-4626
Qubit dsDNA HS Assay kit	Life Technologies	Cat#Q32854
Nextera XT Sample Preparation kit	Illumina	Cat#FC-131-10
FOXP3 staining buffer set kit	eBioscience	Cat#00-5523-00
$CD4^+CD25^+$ T-regs Isolation kit	Miltenyi Biotec	Cat#130-091-301
CellTrace™ CFSE Cell Proliferation dye	Thermo Fisher	Cat#C34554
Zenon Pacific Orange Mouse IgG1 labeling kit	Thermo Fisher Scientific	Cat#Z25269
Deposited Data		
RNA sequencing data	European Genome-Phenome Archive (EGA)	EGAS00001002508
Experimental Models: Cell Lines		
CAF-S1	This paper	N/A
CAF-S4	This paper	N/A
Oligonucleotides		
CCL11 F: 5'-CCGACCCCAAGAAGAAGTGG-3'	Eurofins	N/A
CCL11 R: 5'-GCAACACTCAGGCTCTGGTT-3'	Eurofins	N/A
CXCL12β F: 5'-AACAGACAAGTGTGCATTGACCCG-3'	Eurofins	N/A
CXCL12β R: 5'-TAACACTGGTTTCAGAGCTGGGCT-3'	Eurofins	N/A
TNFSF4 F: 5'-CCTCGAATTCAAAGTATCAAAG-3'	Eurofins	N/A
TNFSF4 R: 5'-GTGAGGATGAAACCTTTCTCC-3'	Eurofins	N/A
JAM2 F: 5'-CGCCCTGGGCTATCATAAGG-3'	Eurofins	N/A
JAM2 R: 5'-CAAAGGAGACACTCCGACCC-3'	Eurofins	N/A
PDCD1LG2 F: 5'-ACAGTGCTATCTGAACCTGTGG-3'	Eurofins	N/A
PDCD1LG2 R: 5'-GTCATATCAGGTCACCCTGGC-3'	Eurofins	N/A
CD276 F: 5'-CTGGCTTTCGTGTGCTGGAGAA-3'	Eurofins	N/A
CD276 R: 5'-GCTGTCAGAGTGTTTCAGAGGC-3'	Eurofins	N/A
NT5E F: 5'-CTCCTCTCAATCATGCCGCT-3'	Eurofins	N/A
NT5E R: 5'-TGGATTCCATTGTTGCGTTCA-3'	Eurofins	N/A
DPP4 F: 5'-AGTGGCGTGTTCAAGTGTGG-3'	Eurofins	N/A
DPP4 R: 5'-CAAGGTTGTCTTCTGGAGTTGG-3'	Eurofins	N/A
Cyclophilin B F: 5'-AGGCCGGGTGATCTTTGGTCT-3'	Eurofins	N/A
Cyclophilin B R: 5'-CCCTGGTGAAGTCTCCGCCCT-3'	Eurofins	N/A
siCCL11	Qiagen	Cat#GS6353
siTNFSF4/OX40L	Qiagen	Cat#GS7292
siPDCD1LG2/PD-L2	Qiagen	Cat#GS80380
siJAM2	Qiagen	Cat#GS58494
siCD276/B7H3	Qiagen	Cat#GS80381
siNT5E/CD73	Qiagen	Cat#GS4907
siDPP4	Qiagen	Cat#GS1803
siCXCL12	Dharmacon	Cat#L-00783-00-0005
siCTR, AllStars negative control	Qiagen	Cat#1027281
Software and Algorithms		
SPADE.driver of the spade R library (*version 1.10.4*)		http://www.bioconductor.org/packages//2.12/bioc/html/spade.html
Definiens Tissue Studio	Definiens	http://www.definiens.com
Tophat_2.0.6 algorithm		http://ccb.jhu.edu/software/tophat/index.shtml
DESeq2		https://bioconductor.org/packages/release/bioc/html/DESeq2.html

(*Continued on next page*)

Continued		
REAGENT or RESOURCE	SOURCE	IDENTIFIER
Ingenuity Pathway Analysis	Qiagen	https://www.qiagenbioinformatics.com/products/ingenuity-pathway-analysis/
R versions 3.3.2 and 3.4.0		https://cran.r-project.org
ImageJ		https://imagej.nih.gov/ij
MOSAIC ToolSuite		http://mosaic.mpi-cbg.de/?q=downloads/imageJ
GraphPad Prism software	GraphPad	https://www.graphpad.com
FlowJo version 9.8.1	LLC	https://www.flowjo.com/solutions/flowjo
Other		
HyClone	HyClone	Cat#SH30243.01
CO_2-independent medium	Gibco	Cat#18045-054
Human serum	BioWest	Cat#S4190-100
Sodium Pyruvate	Gibco	Cat#11360-088
Non-essential amino acids 100X	Gibco	Cat#11140-068
TexMACS medium	Miltenyi Biotec	Cat#130-097-374

CONTACT FOR REAGENT AND RESOURCE SHARING

Further information and requests for resources should be directed to, and will be fulfilled by the Lead Contact, Fatima Mechta-Grigoriou (Fatima.Mechta-Grigoriou@curie.fr).

EXPERIMENTAL MODEL AND SUBJECT DETAILS

Cohorts of Breast Cancer Patients

The projects developed here are based on surgical residues, available after histopathological analyses, and not required for diagnosis. There is no interference with clinical practice. Analysis of tumor samples was performed according to the relevant national law on the protection of people taking part in biomedical research. All patients included in our study were female and were informed by their referring oncologist that their biological samples could be used for research purposes and they gave their verbal informed consent. In case of patient refusal, that could be either orally expressed or written, residual tumor samples were not included in our study. Human experimental procedures were approved by the Institutional Review Board and Ethics committee of the Institut Curie Hospital group (approval February 12th, 2014) and CNIL (Commission Nationale de l'informatique et des Libertés) (No approval: 1674356 delivered March 30th, 2013). HER2-amplified carcinomas have been defined according to ERBB2 immunostaining using ASCO's guideline. Luminal (Lum) tumors were defined by positive immunostaining for ER (Estrogen receptor) and/or PR (Progesterone receptor). The cut-off used to define hormone receptor positivity was 10% of stained cells. Among invasive ductal carcinomas, the TN immunophenotype was defined as follows: ER^-PR^- $ERBB2^-$ with the expression of at least one of the following markers: $KRT5/6^+$, $EGF\text{-}R^+$, Kit^+. The mean age of patients at diagnostic, histological grade, pathological tumor size, pathological lymph node status, pathological metastasis status, BC subtypes and tumor size indicated are established at time of diagnostic.

Prospective Cohort

BC specimens were collected from patients at diagnosis, prior any treatment to avoid any side effect of therapies on CAF composition. For each patient, two specimens, corresponding to the tumor and juxta-tumor were included in this study, after evaluation by a pathologist. Patients included were exempt of any therapy, including anti-inflammatory treatment at least one month before surgery. CAF subsets were analyzed from fresh BC samples by fluorescence-activated cell sorting (FACS) (18 patients) or RNA sequencing (16 patients). Prospective cohorts include Lum and TNBC subtypes.

Retrospective Cohorts

An exploratory and a validation cohorts composed of 60 and 272 BC patients, respectively, have been studied, mainly for IHC analyses. Retrospective cohorts include LumA, HER2 and TNBC subtypes. IHC were performed on residual surgery samples prior any treatment. Clinical features of prospective and retrospective cohorts are described in detail in Table S1.

Isolation and Culture of Primary CAF

Fresh BC from female patients received after surgery were cut into fragments of approximately 1 mm^3, put in petri dishes and cultured in DMEM (HyClone #SH30243.01) supplemented with 10% FBS (PAA, #A11-151), streptomycin (100 μg/ml) and penicillin (100 U/ml) (Gibco #15140122) for 2-3 weeks at 37°C. Media was renewed every 3 days. When fibroblast-like cells were visible of confluence at least 50%, they were detached with trypsin, washed and centrifuged (5 min 1000 rpm) and plated in new plates using DMEM supplemented as above, being this passage one. All experiments were performed with fibroblasts until passage 10 to avoid CAF

senescence. Verification of the identity of CAF-S1 and CAF-S4 cells was determined by flow cytometry. Briefly, primary CAF cells were trypsinized from culture dishes (around 500 000 CAF), resuspended in complete medium and after centrifugation, the pellet was resuspended in PBS+ solution. Cells were then stained with LIVE/DEAD™ Fixable Aqua Dead Cell Stain dye (ThermoFisher Scientific, #L34957) diluted in PBS for 20 min at RT and fixed in PFA 4% for 20 min at RT. After a rapid washing step in PBS+ solution, cells were incubated for 45 min at RT with the antibody cocktail in PBS+ supplemented with 0.1% saponin or with the corresponding isotype cocktail. The antibody cocktail contains anti-EpCAM-BV605 (BioLegend, #324224), anti-CD31-PECy7 (BioLegend, #303118), anti-CD45-APC-Cy7 (BD Biosciences, #BD-557833), anti-CD29-Alexa Fluor 700 (BioLegend, #303020), anti-FAP-APC (primary antibody, R&D Systems, #MAB3715 and fluorescent dye Zenon APC IgG1 labeling kit, Thermo Fisher Scientific, #Z25051), anti-PDGFRβ-BV405 (BD Biosciences, #BD-564124), anti-SMA-AlexaFluor594 (R&D systems, #IC1420T), anti-FSP1-PE (BioLegend, #370004), anti-DPP4-BV650 (BD Biosciences, #744451). For data acquisition and analysis, see #*Cell isolation from BC specimens*. 50 000 events per sample were recorded.

METHOD DETAILS

Flow Cytometry and Cell Sorting

Cell Isolation from BC Specimens

Fresh human samples (tumors and juxta-tumors) were obtained from the operating room, after specimen's macroscopic examination and selection of areas of interest for diagnosis by a pathologist. BC samples were cut into small fragments (around 1 mm^3) and digested in CO_2-independent medium (Gibco, #18045-054) supplemented with 5% fetal bovine serum (FBS, PAA, #A11-151), 2 mg/ml collagenase I (Sigma-Aldrich, #C0130), 2 mg/ml hyaluronidase (Sigma-Aldrich, #H3506) and 25 μg/ml DNase I (Roche, #11284932001) for 45 min at 37°C with shaking (160 rpm). After tissue digestion, cells were filtered using a cell strainer (40 μm, Fischer Scientific, #223635447) and resuspended in PBS+ solution (Gibco, #14190) supplemented with 2 mM EDTA (Gibco, #15575) and 1% Human serum (BioWest, #S4190-100) to a final concentration at approximately $5x10^5$ cells in 50 μl.

FACS Gating Strategy for CAF Subsets Identification

BC cells were stained with an antibody cocktail containing anti-EpCAM-PerCR/Cy5.5 (BioLegend, #324214), anti-CD31-PECy7 (BioLegend, #303118), anti-CD45-APC-Cy7 (BD Biosciences, #BD-557833), anti-CD29-Alexa Fluor 700 (BioLegend, #303020), anti-FAP-Pacific Orange (primary antibody, R&D Systems, #MAB3715), anti-PDGFRβ-PE (BioLegend, #323606) and anti-Caveolin1-FITC (Santa Cruz, #70516) for surface staining and anti-SMA-APC (R&D Systems, #IC1420A) and anti-FSP1-Alexa Fluor 647-R-PE (primary antibody, Abcam, #ab27957) for intracellular staining. Most of the antibodies were purchased already conjugated with fluorescent dyes except the anti-FAP and anti-FSP1 antibodies, which were conjugated with fluorescent dye Zenon Pacific Orange Mouse IgG1 labeling kit (Thermo Fisher Scientific, #Z25269) and with fluorescent dye Alexa Fluor 647-RPE conjugated with a goat anti-rabbit Rabbit IgG secondary antibody (Thermo Fisher Scientific, #A-20991), respectively. Isotype control antibodies for each CAF marker used were: iso-anti-CD29 (BioLegend, #400144), iso-FAP (primary antibody, R&D Systems, #MAB002), iso-anti-PDGFRβ (BioLegend, #400114), iso-anti-CAV1 (Santa Cruz, #2857), iso-anti-SMA (R&D Systems, #IC003A) and iso-anti-FSP1 (primary antibody, Abcam, #ab27472). For intracellular staining, cells were incubated with violet LIVE/DEAD dye (Thermo Fisher Scientific, #L34955) for 20 min at room temperature (RT) in PBS (Gibco, #14190) to exclude dead cells, and then fixed in 4% paraformaldehyde (PFA, Electron Microscopy Sciences, #15710) overnight (ON) at 4°C. After a rapid washing step in PBS+ solution, cells were incubated for 45 min at RT with the antibody cocktail in PBS+ supplemented with 0.1% saponin (Sigma-Aldrich, #S7900).

Flow Cytometry Analysis

For surface and intracellular staining, cells were analyzed on the LSRFORTESSA analyzer (BD biosciences). At least 5 x 10^5 events were recorded. Compensations were performed using single staining on anti-mouse IgG and negative control beads (BD bioscience #552843) for each antibody and on ArC reactive beads (Molecular probes #A10346) for Live/Dead staining. Data analysis was performed using FlowJo version 9.8.1 (LLC, USA). Cells were first gated based on forward (FSC-A) and side (SSC-A) scatters (measuring cell size and granulosity, respectively) to exclude debris. Single cells were next selected based on SSC-A versus SSC-W parameters. Dead cells were excluded based on their positive staining for Live/Dead (fixed conditions) or DAPI (surface staining). Cells were then gated on $EpCAM^-$, $CD45^-$, $CD31^-$ cells, for excluding epithelial cells ($EpCAM^+$), hematopoietic cells ($CD45^+$) and endothelial cells ($CD31^+$). $DAPI^-$ $EPCAM^-$, $CD45^-$, $CD31^-$ cells were next examined using the 6 CAF markers including CD29, FAP, SMA, FSP1, PDGFRβ and CAV1. Sorting of CAF subsets after surface staining was performed on FACSARIA (BD biosciences). Spanning-tree progression analysis of density-normalized events (SPADE) algorithm was applied to flow cytometry data (Qiu et al., 2011) using Cytobank (Cytobank Inc., Mountain view, CA, USA). SPADE clustering was performed to generate unified trees based on the expression of the 6 CAF markers. SPADE.driver function of the spade R library (*version 1.10.4*) was used with the following main parameters: downsampling target number = 5000, number of clusters = 300, clustering samples = 50000. CAF subset populations were manually annotated. The potential redundancy between the different markers was next performed by removing successively each stromal marker from the input dataset.

Correlation between CAF Subsets and Immune Cells in BC

To correlate CAF subsets with immune content in BC, fresh tissues were collected and digested, as described above. In addition to CAF subsets using markers, as previously described, the following cell types were analyzed: Hematopoietic cells: $CD45^+$, Macrophages: $CD45^+CD14^+CD11b^+HLADR^+$; B-lymphocytes: $CD45^+CD14^-CD3^-CD19^+$; Natural Killer: $CD45^+CD14^-CD3^-CD16^+$;

$CD4^+/CD8^+$ T lymphocytes: $CD45^+CD14^-CD3^+CD4^+/CD8^+$; Dendritic Cells $BDCA1^{+/-}$: $CD45^+CD14^+CD11c^{Hi}HLDR^{Hi}BDCA1^{+/-}$; Plasmacytoïd dendritic cells (pDC): $CD14^-CD3^-CD19^-CD16^-CD11c^-CD4^+DR^+$. CAF subsets and $CD45^+$ were detected by flow cytometry as described above. For the detection of the remaining cell types, the following antibodies and the respective dilution were used: anti-CD45 (BD Biosciences, #BD-557833); anti-CD14 (1:1000, Invitrogen, #Q10013), anti-CD11b (Biolegend,1:20 #101239), anti-HLADR (1:150, Biolegend, #307643), anti-CD19 (1:80, Biolegend, #302239), anti-CD16 (1:20, BDBiosciences, #335035), anti-CD4 (1:20, Miltenyi Biotec, #130092374), anti-CD8 (1:80, Invitrogen, #MHCD0822), CD11c (1:20, BDBiosciences, #551077), BDCA1 (1:300, Biolegend, #331506).

Screening of Cytokines from Tumor Supernatants

The tumor supernatants were recovered as follows: tumors (cut into15-20 mg weight fragments) were incubated 24h at 37°C in culture medium (RPMI 1640 Glutamax (Gibco, #61870-044) supplemented with 10% FBS (HyClone #CH30160.03), 1mM Sodium Pyruvate (Gibco, #11360-088), 10 ml Non-essential amino acids 100X (Gibco, #11140-068) and 1% of Penicillin/Streptomycin (Penicillin 10.000U/ml; Streptomycin 10.000 μg/ml, Gibco, #15140-163). After incubation, the supernatants were diluted 1:2 (v/v) in culture media (description above), filtered (pore size of 0.22 μm) and frozen in aliquots at -80°C. Human Milliplex Map kits (Human cytokine/chemokine Magnetic Bead panels I, II, III (Millipore, #HCYTOMAG, #HCYP2MAG, #HCYP3MAG) were purchased from Millipore and used according to manufacturer's recommendations. A multiplex Luminex assay was used to measure the following cytokines simultaneously in the supernatants: IL-1β, IL-2, IL-4, IL-5, IL-6, IL-9, IL-10, IL-13, IL-15, IL-17F, IL-17A, IL-17E, IL-21, IL-22, IL-28A, IL-31, IL-33, IFN-γ, TNF-α, TNF-β, GM-CSF in accordance with manufacturer guidelines (Millipore). The detection limit was 16pg/ml for IL-33 and IL-21, and 4pg/ml for the other measured cytokines.

Immunohistochemistry (IHC)

Formalin-fixed paraffin embedded (FFPE) tissues from BC patients (retrospective cohorts) were cut in serial sections (5 μm). The FFPE sections were prepared for staining using standard protocols for xylene and alcohol gradient for deparafination in the (Sakura, Tissue-Tek DRS). All the stainings were performed in the Lab Vision IHC stainer Autostainer 480 (Thermo Scientific). Antigen retrieval was performed in the microwave for 20 min at 97°C using target retrieval solution citrate pH 6 (Dako, #S2369) or solution pH 9 (Dako, #S2367) according to the primary antibody used, followed by 5 min blockade of endogenous peroxidase activity with Dako REAL peroxidase-blocking solution (Dako, #S202386). Blocking step was made with horse (VECTOR laboratories, #PK-6102 kit) or goat serum (VECTOR laboratories, #PK-6101 kit) diluted 1:50 in PBS supplemented with 1%BSA, depending on the secondary antibody used (horse anti-mouse or goat anti-rabbit, respectively) for 10 min. The tissue sections were then incubated with the primary antibody for 1 h at RT, followed by wash with 1X PBST (Dako, #K8000). Next, the horseradish peroxidase (HRP)-conjugated secondary antibodies horse anti-mouse (VECTOR laboratories, #PK-6102 kit) or goat anti-rabbit (VECTOR laboratories, #PK-6101 kit) were incubated for 25 min at RT. The tissue sections were washed using PBST and then signal detection was performed by incubation with avidin-horseradish peroxidase (Vector Laboratories) for 25 minutes and detected with 3,3'-diaminobenzidine for 5 min (DAB, Dako, #K3468). Counterstaining was performed with Mayer hematoxylin freshly prepared (Dako, #S3309). Tissue sections were then submitted to serial gradients of xylen prior and mounted with coverslip in an automatic device (Sakura, Tissue-Tek DRS). For the validation cohort, the procedures were as described above with minor modifications. BC tissues were on Tissue-Micro-Arrays (TMA) using 2 cores of tumor per case and cut in serial sections of 2 μm. The epitope retrieval was performed in EnVision FLEX Target Retrieval Solution (high- or low-pH, as required, Dako, #K800421 or #K800521) and antigen detection using the EnVision FLEX/HRP (Dako, #K8006). For detecting CAF markers, the following antibodies and respective dilutions were used: anti-CD29 (1:100, Abcam, #ab3167), anti-FAP (1:200, Abcam #ab53066, exploratory cohort and 1:100, Vitatex, #MABS1001, validation cohort), anti-FSP1 (1:250, Abcam, #ab27957), anti-PDGFRβ (1:100, Abcam, #ab32570), anti-SMA (1:200, Dako, #M0851), anti-CAV1 (1:100, BD Biosciences, #610060) and anti-MCAM/CD146 (1:500, Sigma, #HPA008848). For immune markers, the following antibodies were used: anti-CD3 (1:100, Dako, #M7254), anti-CD8 (1:100, Dako, #M4103) and anti-FOXP3 (1:100, Abcam, #ab20034). For evaluation of blood vessel density, the anti-CD31 (1:100, Dako, #M0823) was used. The respective isotype controls, for corresponding IgG and concentration of the primary antibody, were used. Staining overview of the sections was done in the Zeiss Axioplan microscope and slides were then scanned using the Philips Ultra Fast Scanner and visualized at high resolution in the Philips IMS 2.2 software for further analyses and photos. The staining of CAF markers was evaluated using histological scoring, with Histological score = intensity of the staining (0-4) x % fibroblasts stained. To take in consideration the % of stroma in a given tumor sample, and thus analyze not only the activity but also the quantity of this activated stroma, we additionally calculated the C2 HScore, as the product of HScore of each marker x % of stroma per tumor of each tumor. The evaluation of CAF markers using the HScores as described above was done in all the tumor tissue section in an Axioplan microscope (Zeiss). The readings of the CAF markers were performed by two independent experiments. For quantification of immune cells, the scanned slides were submitted to Definiens Developer application, where all the tissue section, regardless the localization of the immune cells was used for quantification. Quantifications were also performed in the tumor bed and tumor front, the last being defined by pathologists as the area surrounding the tumor bed. For quantification of immune cells in the epithelial or stromal compartments separately, at least 5 to 10 representative fields at 20X magnification per tumor were counted manually and divided by the area of the section considered in a blind manner.

Triple-Immunofluorescence Staining on BC Sections

Sections of FFPE BC (3 μm) were deparaffinated, dehydrated and antigen-retrieved (pH 6, Dako, #S2369) using standard protocols described above. The detection of OX40L or PD-L2 was done using the AlexaFluor647 Tyramide SuperBoost Kit Goat anti-rabbit IgG (Invitrogen, #B40926) and performed according to manual guidelines. Briefly, sections were blocked 2h at RT followed by incubation overnight of primary antibodies: anti-OX40L (1:50, Cell Signaling, rabbit anti-Human #59036) or PD-L2 (1:50, Sigma, rabbit anti-Human #HPA013411) with anti-CD25 (1:50, Invitrogen, mouse anti-Human #MA5-12680) in PBS-T supplemented with 1%BSA. Next, sections were washed twice for 10 min in PBS and then detected with HRP-conjugated streptadivin and tyramide labeling. To do so, the tissue was incubated with 100 μl of freshly prepared tyramide working solution (100X Tyramide stock solution (1:100),100X H_2O_2 solution (1:100) and 1X Reaction buffer, all provided by the manufacturer) and incubated for 5 to 10 min at RT. Reaction was stopped by addition of Reaction Stop reagent (100 μl) also provided in the kit. Tissue sections were washed three times with PBS. Detection of CD25 was performed using anti-mouse Alexa488 (1:300, Invitrogen, #A11001) during 30 min at RT and washed twice for 10 min in PBS. Finally, sections were then labeled for FAP (1:100, Vitatex, rat anti-Human #MABS1001) during 1h at RT and detected using anti-rat Cy3 secondary antibody (1/300, Jackson ImmunoResearch Laboratories, #712-165-153) during 30 min. Sections were then mounted with using Vectashield with DAPI mounting media (Vector Laboratories, #H-1200). Images were acquired at 40X on HistoFluor microscope (Nikon).

Design of a Decision Tree for CAF Subset Prediction

CAF identity was determined by using an algorithm developed by the team, which takes as input histological scores of CAF markers. The thresholds were first defined, in a learning dataset, on the distribution (1st quartile, median and 3rd quartile) of each marker using FACS data. Thresholds were then transposed to IHC data.

Sensitivity Analysis of the CAF Decision Tree

The decision tree-based classifier of CAF subtypes was tested for misclassification rate with respect to possible significant uncertainty in the values of its input variables, using sensitivity analysis. First, we applied Monte Carlo one-variable-at-a-time approach (Saltelli et al., 2004) with uniform random sampling (N=1000) of each variable for each data point. The random sampling changed the variable at maximum two-fold both in the direction of increase and decrease of the value. In other words, we assumed possible uncertain measurement with any value from half to two times of the actual variable value. Finally, we estimated the misclassification rate (classification sensitivity) as the fraction of mistakes in the class assignment using the decision tree for a set of measurements with randomly changed variable, for each fibroblast class separately. Second, in order to quantify interactions between the variables in the decision tree model, we applied the same procedure but varying two variables at a time. The interaction was quantified as $I(\mathrm{var1},\ \mathrm{var2}) = |\mathrm{sensitivity2}(\mathrm{var1}, \mathrm{var2}) - (\mathrm{sensitivity}(\mathrm{var1}) + \mathrm{sensitivity}(\mathrm{var2}))|$, where *sensitivity()* is univariate sensitivity estimated at the previous step, and *sensitivity2()* is the bi-variate sensitivity obtained by varying two variables.

Visualization of CAF Subsets *In Situ* at Cellular Level

IHC staining from consecutive sections were scanned on Philips Ultra Fast Scanner. 10X images of each of the CAF markers (CD29, FAP, PDGFRβ, SMA, FSP1) from the same tumor areas in representative tumors were further analyzed. Images were aligned using elastic transformation from Fiji software plugin (bUnwarpJ). This plugin uses landmarks manually defined on haematoxilin & eosin (H&E) staining of the sections to compute the optimal correlation between images and aligned at cellular level by elastic transformation. Images were divided into tiles of 225 μm^2 to mimic the approximate size of one fibroblast and each tile was annotated according to the position in the section. Aligned and annotated images of the CAF markers were then submitted to color deconvolution and the intensity of each DAB staining was measured by densitometry analysis using ImageJ software. Each tile was classified into a specific CAF subset using the algorithm developed by the team (see previous paragraph), which takes as input DAB intensities of CAF markers measured within each tile. Epithelial tumor cells were masked (represented in grey or black) to better visualize the stromal compartment and each tile was colored according to the classification into CAF-S1 to CAF-S4, using the scheme colors defined throughout this study: CAF-S1 red, CAF-S2 orange, CAF-S3 green and CAF-S4 blue.

RNA Sequencing of CAF-S1 and CAF-S4 Sorted from BC

Fresh BC tissues and juxta-tumors were processed immediately after-surgery and CAF-S1 and CAF-S4 cellular subpopulations were collected after FACS sorting using the same strategy, as described above (# *Flow cytometry and cell sorting*) using cell surface staining compatible with RNA extraction. 16 Tumors (10 Lum and 6 TN) and whenever possible, the corresponding juxta-tumors (12) were included in the analysis. In total, 28 CAF-S1 and 19 CAF-S4 cell populations were FACS sorted and collected in non-stick RNase-free tubes (Thermo Fisher Scientific #AM12450). A minimum of 100 cells were collected for each CAF subset from fresh BC. After sorting, cells were immediately processed for total RNA extraction using the Single Cell Purification kit (Norgen Biotek, #51800) following the manual instructions. RNA integrity and quality were analyzed with the Agilent RNA 6000 Pico kit (Agilent Technologies, #5067-1513). cDNA Synthesis and amplification was prepared using the SMARTer Ultra Low Input RNA kit (Clontech, #634826). cDNA quality was verified with Agilent High Sensitivity DNA kit (Agilent Technologies, #5067-4626) and quantified using the Qubit dsDNA HS Assay kit (Life Technologies, #Q32854). cDNA library was prepared using the Nextera XT Sample Preparation kit (Illumina, #FC-131-10) followed by sequencing on a rapid run flow cell of HiSeq 2500 (Illumina). Average sequencing depth was of 30 millions of paired-end reads, with read length of 100bp. Reads were mapped on the reference genome (hg19/GRCh37 from UCSC genome release)

using Tophat_2.0.6 algorithm with the following parameters: global alignment, no mismatch in seed alignment (size 22) and 3 mismatches in read length. Quality control was performed using FastQC software and duplicates were removed using Samtools rmdup. Quantification of gene expression was performed using HTSeq-count and featureCounts (implemented in Bioconductor R package Rsubread). Only genes with one read in at least 5% of all samples were kept for further analyses. Normalization was done using the method implemented in DESeq2 R package. Analysis strategy includes unsupervised analysis such as PCA and HC, as well as differential expression analysis (done with DESeq2 bioconductor package). Biological interpretations of genes were assessed by Gene Ontology (GO), Kyoto Encyclopedia of Genes and Genomes (KEGG) databases, using DAVID bioinformatics resources (https://david-d.ncifcrf.gov) and from Ingenuity Pathway Analysis (IPA) software.

Design of the Map Showing CAF Molecular Interactions

The map of molecular interactions in CAFs was created for data visualization and functional analysis of the results of transcriptomics data analysis. This interactive network map (available online: https://navicell.curie.fr/navicell/newtest/maps/caf/master/index.html) is based on the manual curation by the biocurators of the information about CAF-specific molecular mechanisms from scientific literature and external databases, using established methodology previously developed and validated (Kuperstein et al., 2015). The biocuration process focused on extracting CAF-specific interactions from the original publications and the reviews. The map was constructed using Systems Biology Graphical Notation standard (SBGN) as implemented in CellDesigner tool that ensures compatibility of the maps with various tools for network analysis, data integration and network modelling. Each molecular player and each reaction on the map is annotated using NaviCell annotation format. The annotations include literature references, cross-references with other molecular biology databases and the notes of the biocurator in a free text format. In addition, a detailed system of tags is used in order to annotate the map components indicating their participation in different functional modules representing the key roles of CAFs in TME. The map is divided into 11 functional modules: ''Integrin signaling pathways'', ''Motility'', ''Matrix regulation'', ''Growth factors production'', ''Interaction with tumor cells'', ''Markers of fibroblast activation'', ''Treg modulators'', ''Cytokines and chemokines production'', ''Inflammatory signaling pathways'', ''Core signaling'', ''Growth factors signaling pathways''. The map describes 681 chemical species (post-translational modifications of 303 proteins and 87 genes) connected by 581 reactions. The construction of the map was based on 358 manually curated articles including 50 reviews, the majority of which are published during the 2010-2016 period.

Visualizing Transcriptomic Data on Top of the Comprehensive Molecular Interaction Map

The CAF map was applied for data analysis and visualization of the CAF-S1 and CAF-S4-specific RNAseq data. The log-scaled expression of each gene was centered across all CAF samples such that the globally average expression of any gene became zero. The average centered expression values of all genes composing the functional modules of the CAF map were used to define a score associated to each functional module. This score was visualized on top of the map using the ''Stain CellDesigner map'' function from BiNoM Cytoscape plugin using red-green color scale.

RNA Extraction, cDNA Synthesis and qRT-PCR

Cultured primary CAF-S1 were lysed in Trizol and RNA were isolated using miRNeasy kit (Qiagen, #21704) and Qiacube, following manufacturer's instructions. RNA was quantified using a Nanodrop apparatus and 1 μg was used for reverse-transcription using random primers (iScript cDNA Synthesis kit; Bio-Rad, #170-8891). For quantitative RT-PCR (qRT-PCR), the *Power* SYBR Green PCR Master Mix (Applied Biosystems, #4367659) and primers at 300 nM (final concentration) were used in a Chromo4 Real-Time PCR detector (Bio-Rad). Primers were designed using an open resource (www.ncbi.nlm.nih.gov/tools/primer-blast). Primer sequences used are listed in the Key Resources Table. Expression levels were normalized to Cyclophilin B and represented as fold change compared to the control (2^(-DDCt)).

Silencing Experiments Using Small-Interfering RNA

For functional assays, primary cultures of CAF-S1 were transfected with a pool of 4 specific siRNAs: siCCL11 (#GS6353), siTNFSF4/OX40L (#GS7292), siPDCD1LG2/PD-L2 (#GS80380), siJAM2 (#GS58494), siCD276/B7H3 (#GS80381), siNT5E/CD73 (#GS4907) and siDPP4 (#GS1803) or non-targeting siRNA (siCTR, AllStarts negative control, #1027281). All siRNAs (FlexiTube Gene Solution siRNA #1027416) and non-targeting siCTR were from Qiagen. For siCXCL12, a pool targeting both α- and β-isoforms was used (Dharmacon, #L-007873-00-0005). Transfections were carried out at a final concentration of 20 nM using DharmaFECT 1 (Dharmacon, #T-2001-02) transfection reagent according to manufacturer's instructions.

Isolation of CD4+CD25+ T Cells and Functional Assays

Isolation of $CD4^+CD25^+$ T Cells

$CD4^+CD25^+$ T lymphocytes were isolated from peripheral blood of healthy donors obtained from the ''Etablissement Français du Sang'', Paris, Saint-Antoine Crozatier blood bank through a convention with the Institut Curie (Paris, France). Briefly, peripheral blood mononuclear cells (PBMCs) were isolated using Lymphoprep (STEMCELL, #07861) as previously described and 500 million PBMC were used for $CD4^+CD25^+$ purification by magnetic cell separation (MACS) with the Human $CD4^+CD25^+$ Tregs Isolation kit (Miltenyi Biotec, #130-091-301) according to manufacturer's instructions. The purity of $CD4^+CD25^+$ T cells purified was determined by flow cytometry.

Transwell Migration Assay

For migration assays, 20 000 cells of CAF-S4, CAF-S1 or CAF-S1 transiently transfected with siCTR, siCCL11, siCXCL12, siCXCL13 or siCXCL14 were plated in 200 μl of DMEM supplemented with 1% FBS, in the lower chamber of the transwell (5 μm pore size, Corning HTS Transwell 96 wells, #CLS3388). $CD4^+CD25^+$ T lymphocytes (175 000 cells in a volume of 50 μl DMEM supplemented with 1% FBS) were plated in the upper chamber and incubated overnight at 37°C. After incubation, T cells in the upper and lower chamber were recovered separately and incubated with 0.5 μl of 10 μm carboxylated beads (Polyscience, #18133) and DAPI (3 μM). T cell counting was performed by FACS using precision beads for normalization and expressed as percentage of migration being the ratio of the T cell number in the lower chamber by the total number of cells. The overall percentage of T cell survival shown is the ratio of T cells alive ($DAPI^-$) by the total number of cells, considering both low and upper chambers. For the attraction of the $CD4^+CD25^+$ T lymphocytes towards chemokines, recombinant human chemokines (Peprotech) were added individually to the lower chamber at the following final concentrations: 10 ng/ml CCL11 (#300-21), 10 μg/ml CXCL12 (#300-28A), 10 ng/ml CXCL13 (#300-47) and 10 ng/ml CXCL14 (#300-50).

Co-culture of T Cells with CAF-S1 Time-Lapse Video Microscopy

For co-culture experiments for time-lapse video microscopy, CAF-S1 (50-60 000 cells) were transiently transfected with siRNA (listed above) and plated in 12-well plates in DMEM supplemented with 10% FBS. Purified $CD4^+CD25^+$ T lymphocytes were freshly added to CAF-S1 cells, 30h post-transfection, to reach a ratio of 1:5 (CAF:T cell). Just before adding the T cells, the media was replaced to DMEM supplemented with 2.5% FBS and immediately placed under a conditioned chamber (37°C) of a Leica video-microscope and recorded for 28 h. Microphotographs were captured in 5 different representative positions every 8 min for each well, resulting in 5 videos per experimental condition generated using Metamorph software.

Analysis of the Time-Lapse Videos

An automatic pipeline, which combines ImageJ plugins and R scripts, was developed to define co-localization between CAF-S1 and $CD4^+CD25^+$ T lymphocytes and follow cell trajectories over time. Normalization was performed by removing median background of all videos. Area of CAF was then evaluated using the ImageJ plugin Phantast (https://github.com/nicjac/PHANTAST-FIJI) with the following parameters: Sigma=1 and Epsilon=0.03. ImageJ plugin Particle Tracker (http://imagej.net/Particle_Tracker) from the MOSAIC ToolSuite (http://mosaic.mpi-cbg.de/?q=downloads/imageJ) was used to detect automatically $CD4^+CD25^+$ T lymphocytes and track immune cells trajectories throughout the video. The following parameters were used: Radius=3, Cutoff=3, Per/Abs=0.1, Link Range=10, Displacement=10. Finally, the exact position of both CAF and T cells was determined and combined for each time-frame allowing detection of co-localization of the two cell types. Two types of interactions between CAF-S1 and T cells were considered based on two parameters, the number of time frames (bin) and the number of minimal contacts (minC) within this time frame window. For each T lymphocyte analyzed, persistent interaction with CAF-S1 was defined as at least 8 contacts observed during a time window of 14 frames (bin=14 and minC=8). All interactions, including short and persistent contacts, were quantified considering at least 1 contact observed during a time window of 10 frames (bin=10 and minC=1). 4 Videos corresponding to 28h (210 frames, 8 min per frame) were analyzed for each condition.

Co-Culture of T Cells with CAF-S1 or CAF-S4 and FOXP3 Induction

To study the impact of CAF-S1 or CAF-S4 on $CD4^+CD25^+$ T cells, we performed co-cultures. 50 000 primary CAF-S1 or CAF-S4 were plated in 24-well plates in DMEM supplemented with 10% FBS and used non-transfected or siRNA-transfected (siCTR, siCD276/B7H3, siNT5E/CD73, siDPP4 and siTNFSF4/OX40L). The medium was replaced by fresh DMEM supplemented with 1% FBS just before 500 000 $CD4^+CD25^+$ T lymphocytes were added to CAF-S4, CAF-S1, or to CAF-S1 + siRNA 30h post-transfection. Co-cultures of CAF-S1 or CAF-S4 and $CD4^+CD25^+$ T cells were incubated for 16 h at 37°C, 20%O_2. Negative control was incubation of $CD4^+CD25^+$ T cells in absence of CAF. After incubation, T cells were collected and analyzed by FACS. In brief, T lymphocytes were incubated with LIVE/DEAD (Thermo Fisher Scientific) for 20 min at RT for exclusion of dead cells. After incubation, cells were washed in PBS+ for 10 min and incubated with an antibody cocktail in PBS+ containing anti-CD45-APC-Cy7, anti-CD3-Alexa Fluor 700 (BD Biosciences, #557943), anti-CD4-APC (Miltenyi Biotec, #130-092-374) and anti-CD25-PE (Miltenyi Biotec, #130-091-024) for 15 min at RT. The detection of FOXP3 was performed using the FOXP3 staining buffer set kit (eBioscience, #00-5523-00) for fixation and permeabilization according to manufacturer's instructions followed by incubation with anti-Foxp3-Alexa Fluor 488 (eBioscience, #53-4776) for 30 min at RT. For CD25 and FOXP3 staining, the corresponding isotype controls were #130-092-215 and #53-4321 for CD25 and FOXP3, respectively. Analyses were performed in the BD LSR II flow cytometer (BD Biosciences) and data was then analyzed using FlowJo version 9.8.1.

Treg Cell Suppressive Assay

Treg Cell Suppressive Assay (adapted from protocol of Benoit Salomon's lab available on protocol exchange (Zaragoza et al., 2016)). CD4+CD25+ were isolated from healthy donor PBMC, as described above. The negative fraction ($CD4^+CD25^-$ cells containing effector T cells, Teff) was also recovered and kept overnight at 4°C in TexMACS medium (Miltenyi Biotec, #130-097-374). $CD4^+CD25^+$ cells were then stained with a pool of fluorescent-conjugated primary antibodies recognizing CD4 (1:20, Miltenyi Biotec, #130-092-374), CD25 (1:40, BD Pharmigen #557741), CD127 (1:20, Thermofisher #11-1278-42), and CD45RA (1:20, BD Pharmigen #555489) proteins together with DAPI. After a washing step, $DAPI^-CD4^+CD25^{high}CD127^-CD45RA^{low}$ cells (enriched in regulatory T cells, Tregs) were sorted on FACSARIA (BD Biosciences) and pre-incubated overnight at 37°C, 5% CO_2, 20% O_2 into 24-well plates, with previously plated 50 000 primary CAF-S1 or CAF-S4 fibroblasts in 1 ml of DMEM supplemented with 1% FBS, or with 1 ml of DMEM supplemented with 1% FBS only (control condition). After 16h of incubation, Tregs were recovered, counted and resuspended in RPMI-1640 medium with 2mM L-glutamine, 10% heat-inactivated FBS, penicillin and streptomycin.

The $CD4^+CD25^-$ cells previously isolated were stained 15 min at 37°C with 1μM CellTrace™ CFSE Cell Proliferation dye (Thermofisher, #C34554) at 1 x 10^7 cells per ml in PBS. Suppression assay was performed in U-bottom 96 well plates (Falcon, #353077) during 4 days at 37°C, 5% CO_2, 20% O_2 in the following conditions: CFSE-stained Teff cells (1 x 10^4 cells/well) were incubated with Treg cells (Treg:Teff ratio, 2:1) preincubated with either CAF-S1 or CAF-S4 fibroblasts, or in medium only (control condition) in presence of anti-CD3/CD28 beads (Gibco, #11131D, 1 x 10^4 beads/well). Wells with CSFE-stained Teffs were used as a negative control of Teff proliferation and shown in Figure 6G, Left (black curve). Wells with CFSE-stained Teffs in presence of CD3/CD28 beads (and in absence of Tregs) were used as a positive control of Teff proliferation and are shown in Figure 6G Left (orange curve), condition referred to "Teffs alone". After 4 days, cells were stained with anti-CD4 antibody (1:20, Miltenyi Biotec, #130-092-374) together with DAPI and analyzed on LSRII analyzer (BD Biosciences). FITC fluorescence (corresponding to CFSE dye) was measured on $DAPI^-CD4^+$ cells. The percentage of suppression was calculated using the formula established in (Zaragoza et al., 2016): ((Log2(y) of Teff alone – Log2(y) of Teff+Treg) / Log2(y) of Teff alone) x 100, where y is the mean fluorescence intensity (MFI) of CFSE on the whole population divided by the MFI of CFSE of non-proliferating cells.

QUANTIFICATION AND STATISTICAL ANALYSIS

Statistical Analysis

The graphical representation of the data and statistical analyses were done using R environment (https://cran.r-project.org) (R versions 3.3.2 and 3.4.0) and GraphPad Prism software. Barplots or scatter plots are represented with mean ± standard error of the mean (sem) from at least three independent experiments. Statistical tests used are in agreement with data distribution: Normality was first checked using the Shapiro–Wilk test and parametric or non-parametric two-tailed test was applied according to normality respect. Association between classes of CAF subsets and clinical features was determined by Fisher's exact test. Time-lapse microscopy videos were analyzed using Kaplan-Meier method and p values were computed by Log-Rank test using survival R package. Statistical tests applied are indicated in the legends. Differences were considered statistically significant when $p \leq 0.05$. In case of multiple testing, p values were adjusted using the Benjamini-Hochberg procedure.

DATA AND SOFTWARE AVAILABILITY

The accession number for the RNAseq data from CAF-S1 and CAF-S4 sorted from BC samples generated in this study is EGAS00001002508.

Cancer Cell, Volume *33*

Supplemental Information

Fibroblast Heterogeneity and Immunosuppressive Environment in Human Breast Cancer

Ana Costa, Yann Kieffer, Alix Scholer-Dahirel, Floriane Pelon, Brigitte Bourachot, Melissa Cardon, Philemon Sirven, Ilaria Magagna, Laetitia Fuhrmann, Charles Bernard, Claire Bonneau, Maria Kondratova, Inna Kuperstein, Andrei Zinovyev, Anne-Marie Givel, Maria-Carla Parrini, Vassili Soumelis, Anne Vincent-Salomon, and Fatima Mechta-Grigoriou

Table S1, Description of the prospective and retrospective cohorts used in the study, Related to Figures 1-4

		Prospective cohorts		Retrospective cohorts		
		Curie (FACS)	Curie (RNAseq)	Exploratory	Validation (all BC subtypes)	Validation (TN BC)
Total number of patients		18	16	60	272	103
Inclusion		2012-2014	2014	1997-2007	2003-2009	2004-2006
Average follow-up (years)		3.4	2.4	4	5.9	5.7
Mean age at diagnosis		64 (40-88)	65 (45-89)	55 (29-89)	56 (26-87)	54 (29-83)
Sample localization						
	Tumor	18	16	60	272	103
	Juxta-tumor	18	12	-	-	-
Histological Grade						
	I	1 (6%)	2 (13%)	18 (30%)	55 (20%)	-
	II	6 (33%)	5 (31%)	4 (7%)	78 (29%)	10 (10%)
	III	5 (28%)	8 (50%)	38 (64%)	139 (51%)	93 (90%)
	NA	6 (33%)	1 (6%)	-	-	-
Pathological tumor Size pT						
	pT0	-	-	-	7 (3%)	7 (7%)
	pT1	6 (33%)	2 (13%)	30 (50%)	70 (26%)	55 (53%)
	pT2	12 (67%)	8 (50%)	28 (47%)	41 (15%)	32 (31%)
	pT3	-	1 (6%)	2 (3%)	8 (3%)	2 (2%)
	pT4	-	-	-	1 (0%)	1 (1%)
	NA	-	5 (31%)	-	145 (53%)	6 (6%)
Pathological Lymph node status pN						
	Negative	10 (56%)	10 (63%)	30 (50%)	104 (38%)	79 (77%)
	Positive	8 (44%)	6 (38%)	26 (43%)	30 (11%)	20 (19%)
	NA	-	-	4 (7%)	138 (51%)	4 (4%)
Metastasis status pM						
	Negative	18 (100%)	10 (63%)	60 (100%)	123 (45%)	98 (95%)
	Positive	-	-	-	-	-
	NA	-	6 (38%)	-	149 (55%)	5 (5%)
Mean tumor size (mm)		31.8	26.5	23.6	19.3	21.7
Subtype						
	LumA	13 (72.2%)	10 (62.5%)	20 (33%)	114 (42%)	-
	Her2	1 (5.5%)	-	19 (32%)	55 (20%)	-
	TN	4 (22.2%)	6 (37.5%)	21 (35%)	103 (38%)	103 (100%)
Hormonotherapy						
	Yes	13 (72%)	11 (69%)	16 (27%)	96 (35%)	-
	No	4 (22%)	5 (31%)	1 (2%)	38 (14%)	-
	NA	1 (6%)	-	43 (72%)	138 (51%)	-
Radiotherapy						
	Yes	16 (89%)	13 (81%)	55 (92%)	255 (94%)	97 (94%)
	No	2 (11%)	3 (19%)	-	4 (1%)	-
	NA	-	-	5 (8%)	13 (5%)	6 (6%)
Chemotherapy						
	Yes	12 (67%)	9 (56%)	36 (60%)	176 (65%)	95 (92%)
	No	5 (28%)	7 (44%)	2 (3%)	76 (28%)	-
	NA	1 (6%)	-	22 (37%)	20 (7%)	8 (8%)

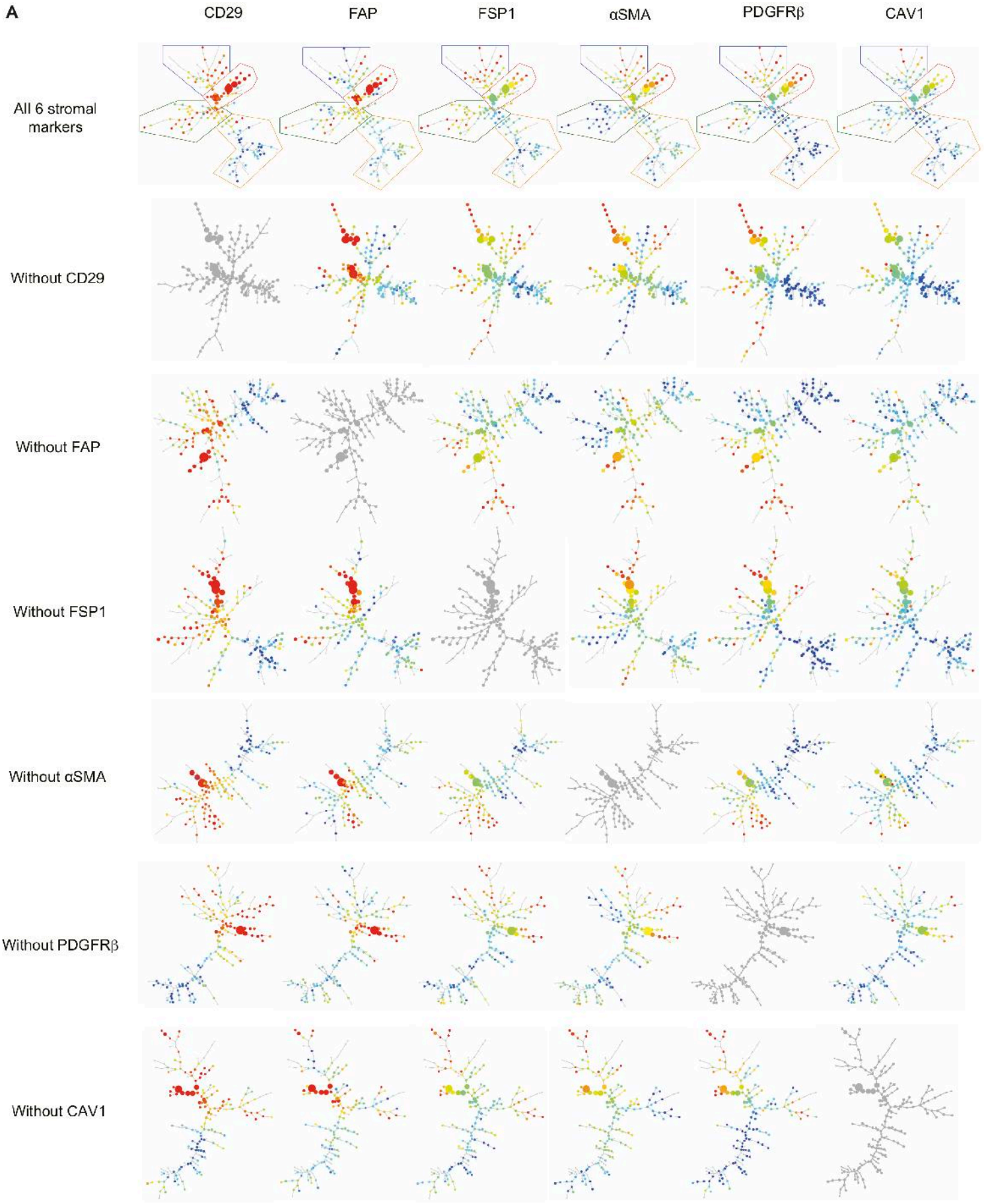
A
CD29
FAP
FSP1
αSMA
PDGFRβ
CAV1
All 6 stromal markers
Without CD29
Without FAP
Without FSP1
Without αSMA
Without PDGFRβ
Without CAV1

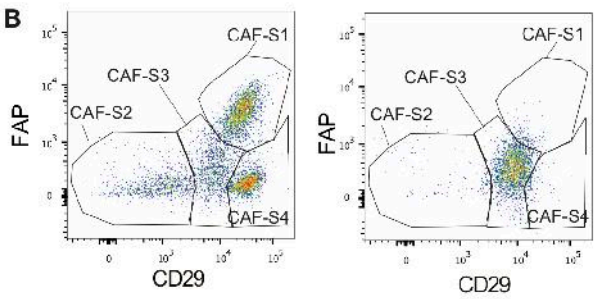
B
CAF-S1
CAF-S3
CAF-S2
CAF-S4
FAP
CD29
CAF-S1
CAF-S3
CAF-S2
CAF-S4
FAP
CD29

Figure S1. Repeated CytoSPADE analysis in absence of each stromal marker, Related to Figure 1.

(A) CytoSPADE trees annotated for each CAF marker expression, as indicated, in BC samples analyzed by FACS (n = 20 BC). Each line shows the CytoSPADE analysis including either the 6 stromal markers (1st line) and next repeated successively in absence of one stromal marker, as indicated. Colors show staining intensities of each marker. Size of the nodes is proportional to the number of cells with similar expression of CAF markers.

(B) Representative pseudocolor flow cytometry plots in Tumor (Left) and Juxta-tumor (Right) on one representative patient, as shown in Figure 1F.

Table S2, Tables of association between CAF subset accumulation and clinical data from FACS prospective cohort and retrospective cohort, Related to Figures 1 and 2

		Prospective cohort (FACS)					Retrospective cohort (all BC)				
		CAF-S1	CAF-S2	CAF-S3	CAF-S4	p value *	CAF-S1	CAF-S2	CAF-S3	CAF-S4	p value *
Histological Grade						0.53					2.31e-11
	I	0	0	0	1		2	24	1	16	
	II	0	2	3	1		8	14	0	33	
	III	0	3	2	0		30	4	2	71	
Subtype						0.35					1.56e-12
	Lum	0	6	6	2		7	39	1	41	
	Her2	-	-	-	-		10	1	0	29	
	TN	1	2	1	0		23	2	2	50	
Pathological tumor size pT						0.14					0.5
	pT0	-	-	-	-		1	0	0	0	
	pT1	0	5	1	0		16	4	2	35	
	pT2	1	3	6	2		7	0	0	25	
	pT3	-	-	-	-		1	0	0	2	
	pT4	-	-	-	-		0	0	0	1	
Pathological Lymph node status pN						0.26					0.4
	Negative	1	5	2	2		21	6	1	47	
	Positive	0	3	5	0		6	0	1	17	
Metastasis status pM						1					1
	Negative	1	8	7	2		25	5	2	59	
	Positive	0	0	0	0		0	0	0	0	
Hormonotherapy						0.47					0.5
	Yes	0	6	6	1		6	33	1	37	
	No	1	2	1	0		3	6	0	13	
Radiotherapy						0.21					0.4
	Yes	1	8	6	1		38	41	3	114	
	No	0	0	1	1		1	0	0	1	
Chemotherapy						0.65					1.65e08
	Yes	1	6	5	0		33	13	2	90	
	No	0	2	2	1		5	27	1	21	

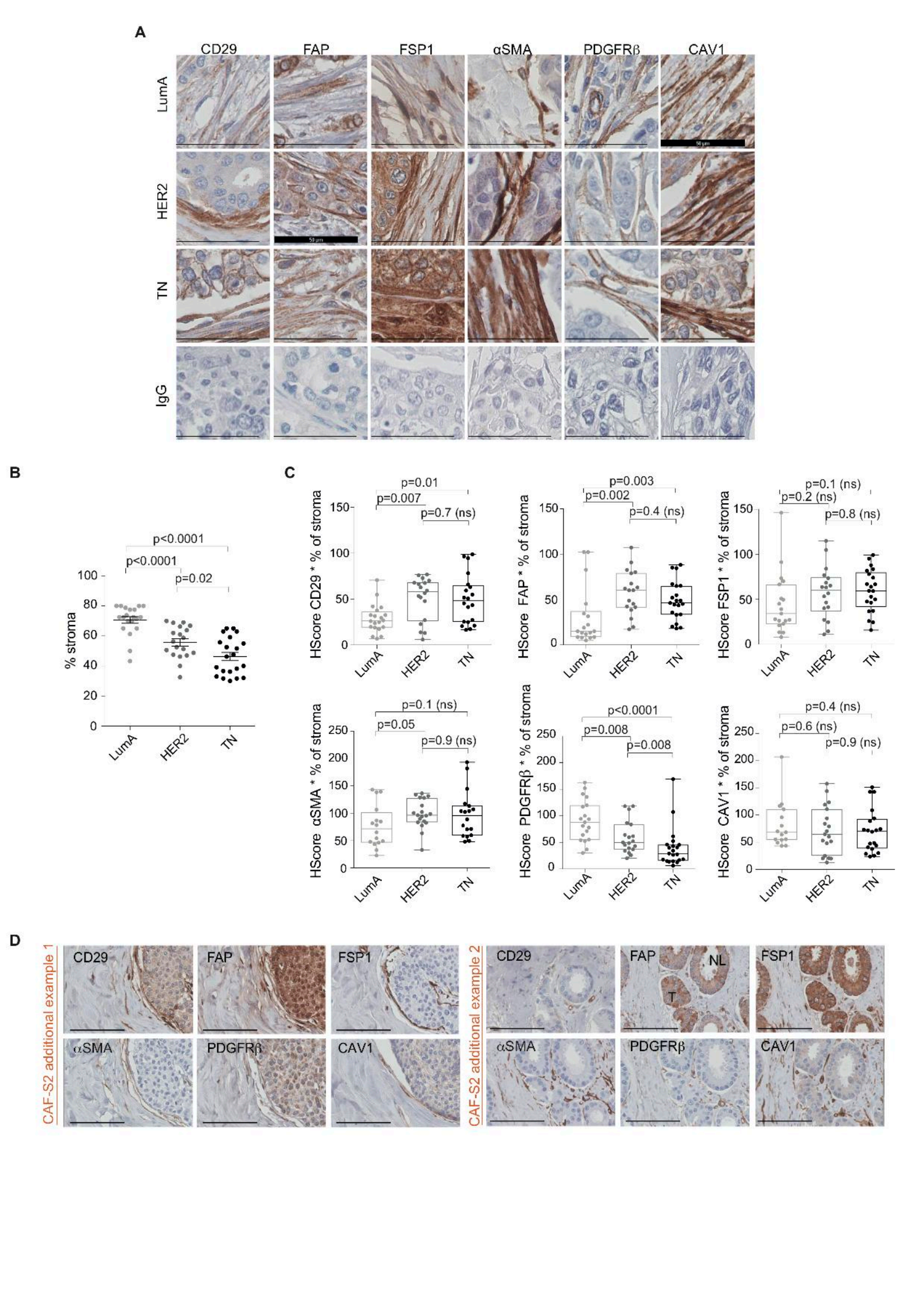
A
CD29
FAP
FSP1
αSMA
PDGFRβ
CAV1
LumA
HER2
TN
IgG
B
% stroma
p<0.0001
p<0.0001
p=0.02
LumA
HER2
TN
C
HScore CD29 * % of stroma
p=0.01
p=0.007
p=0.7 (ns)
HScore FAP * % of stroma
p=0.003
p=0.002
p=0.4 (ns)
HScore FSP1 * % of stroma
p=0.1 (ns)
p=0.2 (ns)
p=0.8 (ns)
HScore αSMA * % of stroma
p=0.1 (ns)
p=0.05
p=0.9 (ns)
HScore PDGFRβ * % of stroma
p<0.0001
p=0.008
p=0.008
HScore CAV1 * % of stroma
p=0.4 (ns)
p=0.6 (ns)
p=0.9 (ns)
D
CAF-S2 additional example 1
CD29
FAP
FSP1
αSMA
PDGFRβ
CAV1
CAF-S2 additional example 2
CD29
FAP
NL
T
FSP1
αSMA
PDGFRβ
CAV1

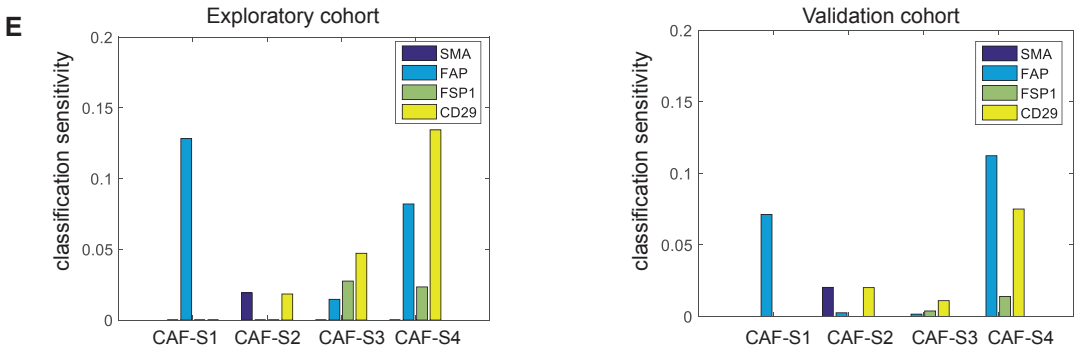
E
Exploratory cohort
Validation cohort
classification sensitivity
SMA
FAP
FSP1
CD29
CAF-S1
CAF-S2
CAF-S3
CAF-S4

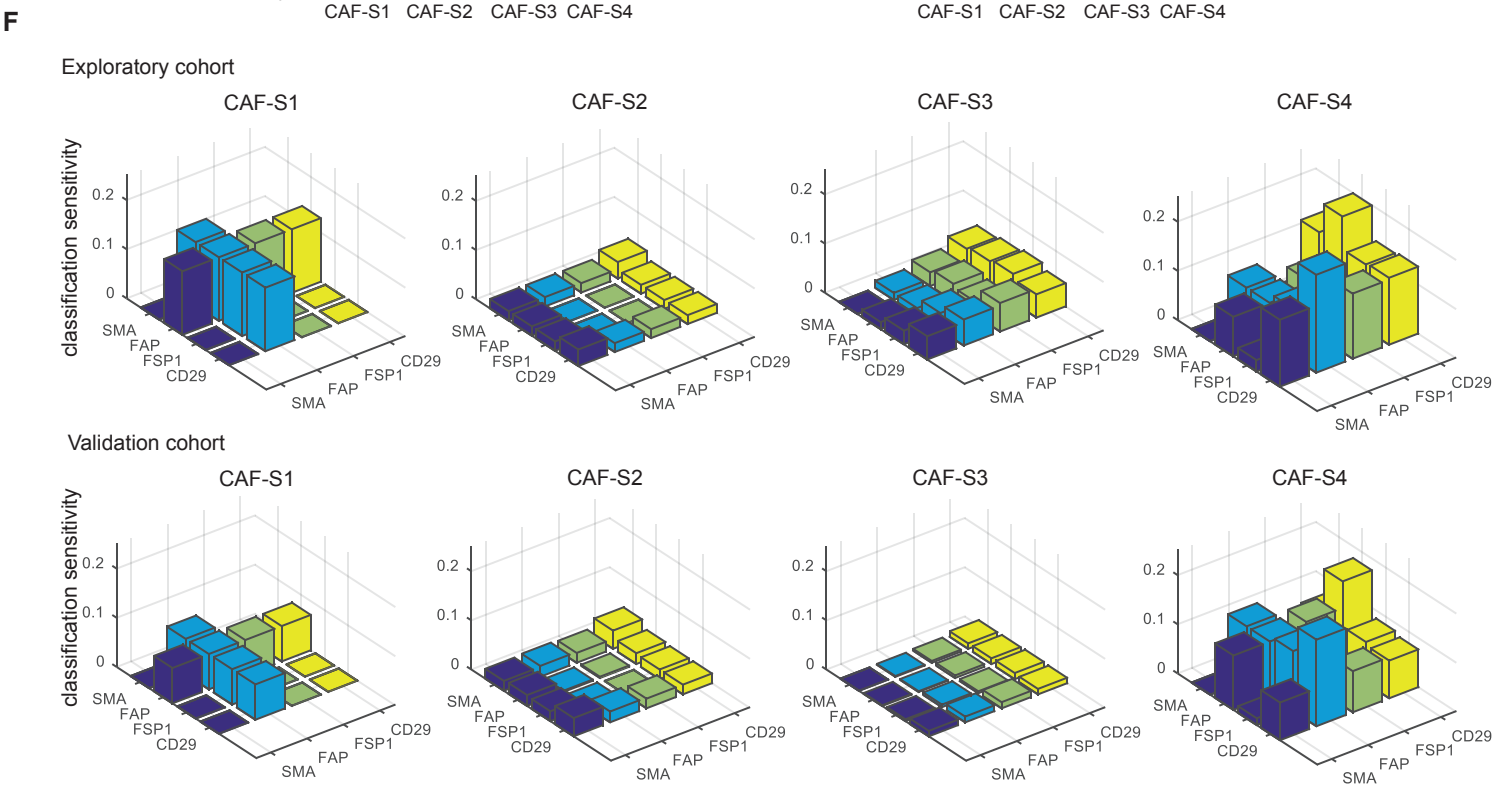
F
Exploratory cohort
Validation cohort
CAF-S1
CAF-S2
CAF-S3
CAF-S4
classification sensitivity
SMA
FAP
FSP1
CD29

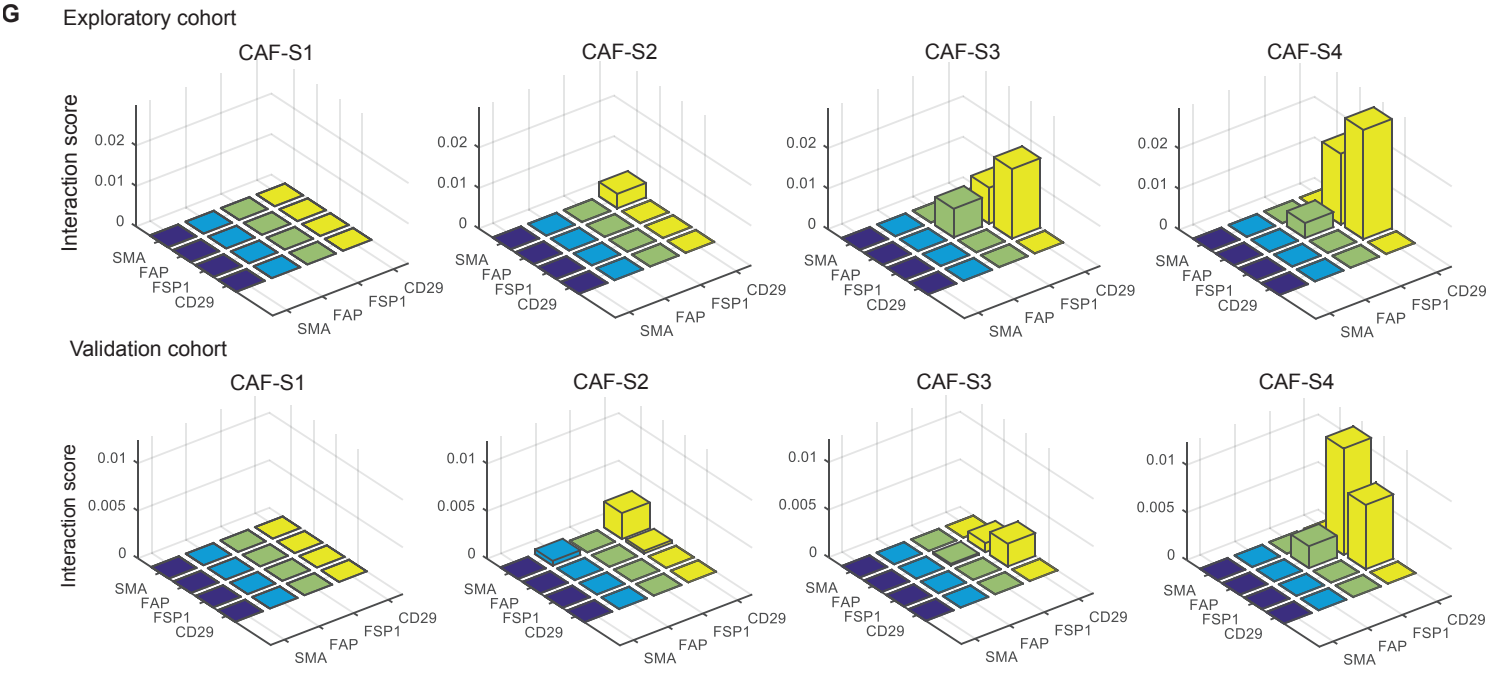
G
Exploratory cohort
Validation cohort
CAF-S1
CAF-S2
CAF-S3
CAF-S4
Interaction score
SMA
FAP
FSP1
CD29

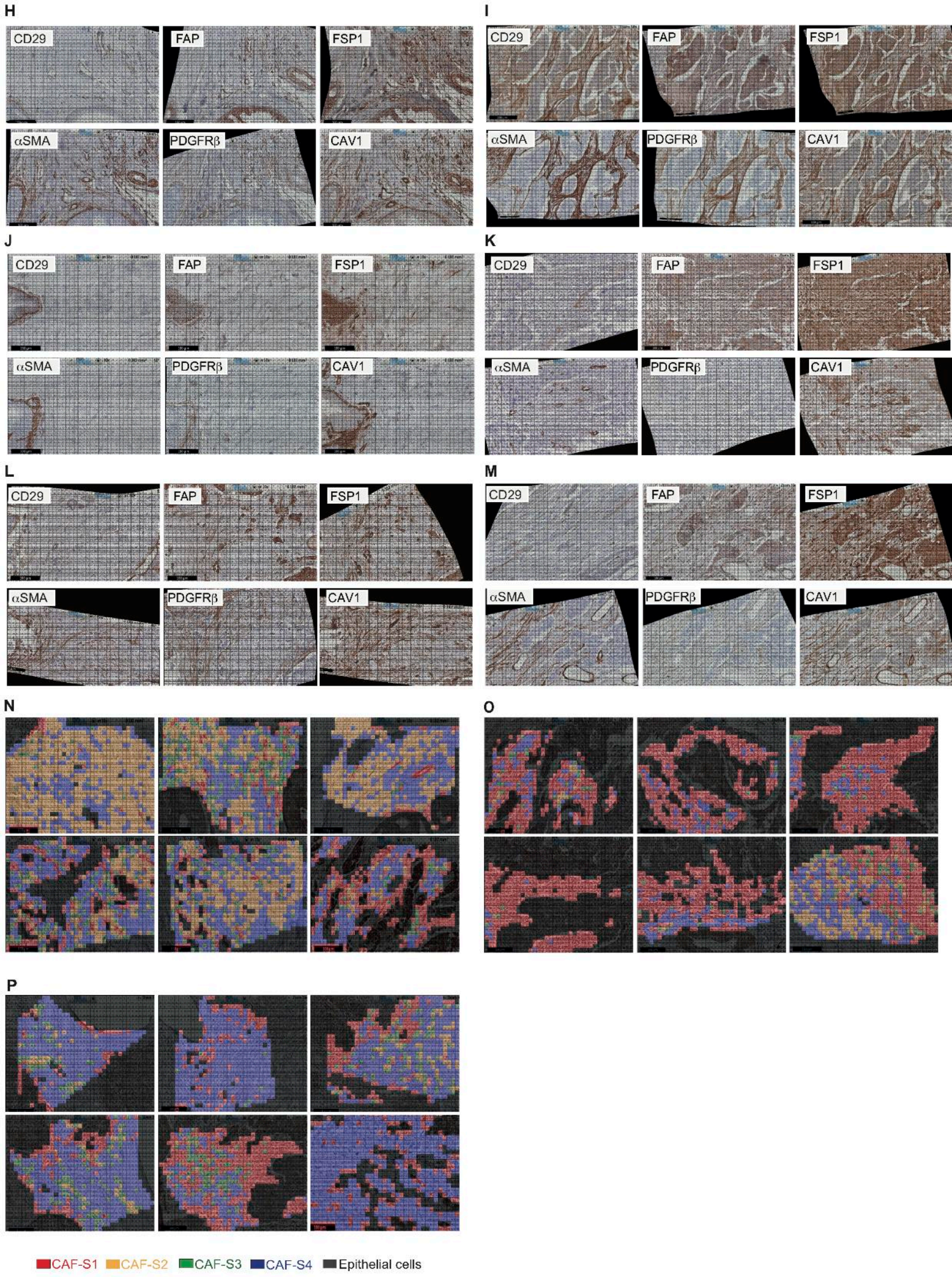
H
CD29
FAP
FSP1
αSMA
PDGFRβ
CAV1
I
CD29
FAP
FSP1
αSMA
PDGFRβ
CAV1
J
CD29
FAP
FSP1
αSMA
PDGFRβ
CAV1
K
CD29
FAP
FSP1
αSMA
PDGFRβ
CAV1
L
CD29
FAP
FSP1
αSMA
PDGFRβ
CAV1
M
CD29
FAP
FSP1
αSMA
PDGFRβ
CAV1
N
O
P
CAF-S1
CAF-S2
CAF-S3
CAF-S4
Epithelial cells

Figure S2. CAF maps and sensitivity analysis evaluating the robustness of the decision tree, Related to Figure 2

(A) Representative views of CD29, FAP, FSP1, αSMA, PDGFRβ, and CAV1 staining by immunohistochemistry (IHC) in tumors of LumA, HER2 and TN BC subtypes from the exploratory cohort. IgG control staining for each antibody used is shown, as appropriate. Scale bar = 50 μm.

(B) Scatter plot showing the percentage of stroma in LumA, HER2 and TN BC subtypes of the exploratory cohort. n = 60 BC (20 LumA, 19 HER2, 21 TN). Data are shown as mean ± SEM. p values are based Mann-Whitney test.

(C) Box and whisker plots showing the C2 histological scores (C2 HScore) per BC subtype. For each CAF marker, HScore is given as a function of the percentage of positive cells multiplied by the staining intensity (ranging from 0 to 4) (as shown Figure 2A). Based on that, the C2 HScore is defined as the product of the HScore of each marker multiplied by the percentage of stroma per tumor. n = 60 BC (exploratory cohort, 20 LumA, 19 HER2, 21 TN). Data are shown as median ± min to max. p values are from Mann-Whitney (CD29, FAP, PDGFRβ, CAV1) or Student (FSP1, αSMA) t-tests, as appropriate.

(D) Representative views of CD29, FAP, FSP1, αSMA, PDGFRβ and CAV1 immunostaining of serial BC sections. Representative BC areas enriched in CAF-S2 subset are shown. Scale bar = 100 μm.

(E) Univariate analysis of model variables, sensitivities are defined as the fraction of misclassified random samples around data points, uniformly changing any model variable by two-fold at maximum in both directions (increase and decrease). The misclassification rate, referred to as classification sensitivity, is thus defined as the fraction of mistakes in the class assignment using the decision tree (shown in Figure 2D) based on CAF marker histological scores with randomly changed variable (N=1000), for each fibroblast class, separately.

(F) Bivariate analysis of classification sensitivities following the random change of 2 CAF marker expressions simultaneously.

(G) Quantification of interactions between model input variables. The interaction was quantified as: /(var1, var2) = |*sensitivity2*(var1,var2) - (*sensitivity*(var1) + *sensitivity*(var2))|, where *sensitivity()* is univariate sensitivity estimated in A, and *sensitivity2()* is the bi-variate sensitivity obtained by varying two variables estimated in B.

(H-M) Representative views of CD29, FAP, FSP1, αSMA, PDGFRβ and CAV1 immunostaining of serial consecutive sections from BC used for defining maps of CAF subsets at cellular scale, shown in Figure 2G. CAF-S2-enriched LumA tumor,

Related to map shown in Figure 2G, Left, Up. CAF-S2-enriched LumA, Related to map shown in Figure 2G, Left, Up (H). CAF-S1-enriched TN tumor, Related to map shown in Figure 2G, Right, Up (I). CAF-S2-enriched LumA, Related to map shown in Figure 2G, Left, Middle (J). CAF-S1-enriched TN tumor, Related to map shown in Figure 2G, Right, Middle (K). CAF-S4-enriched LumA tumor, Related to map shown in Figure 2G, Left, Down (L). CAF-S4-enriched TN tumor, Related to map shown in Figure 2G, Right, Down (M).

(N-P) Additive examples of CAF subset maps at cellular level in LumA and TNBC. Each CAF subset is represented by a color code, as indicated, and epithelial tumor cells are shown in black. These images were reconstructed by applying mathematical modeling (see Methods) on HScores of all CAF markers on serial sections. Examples of CAF subset maps in LumA tumors (N). Examples of CAF subset maps in TNBC enriched in CAF-S1 (O). Examples of CAF subset maps in TNBC enriched in CAF-S4 (P).

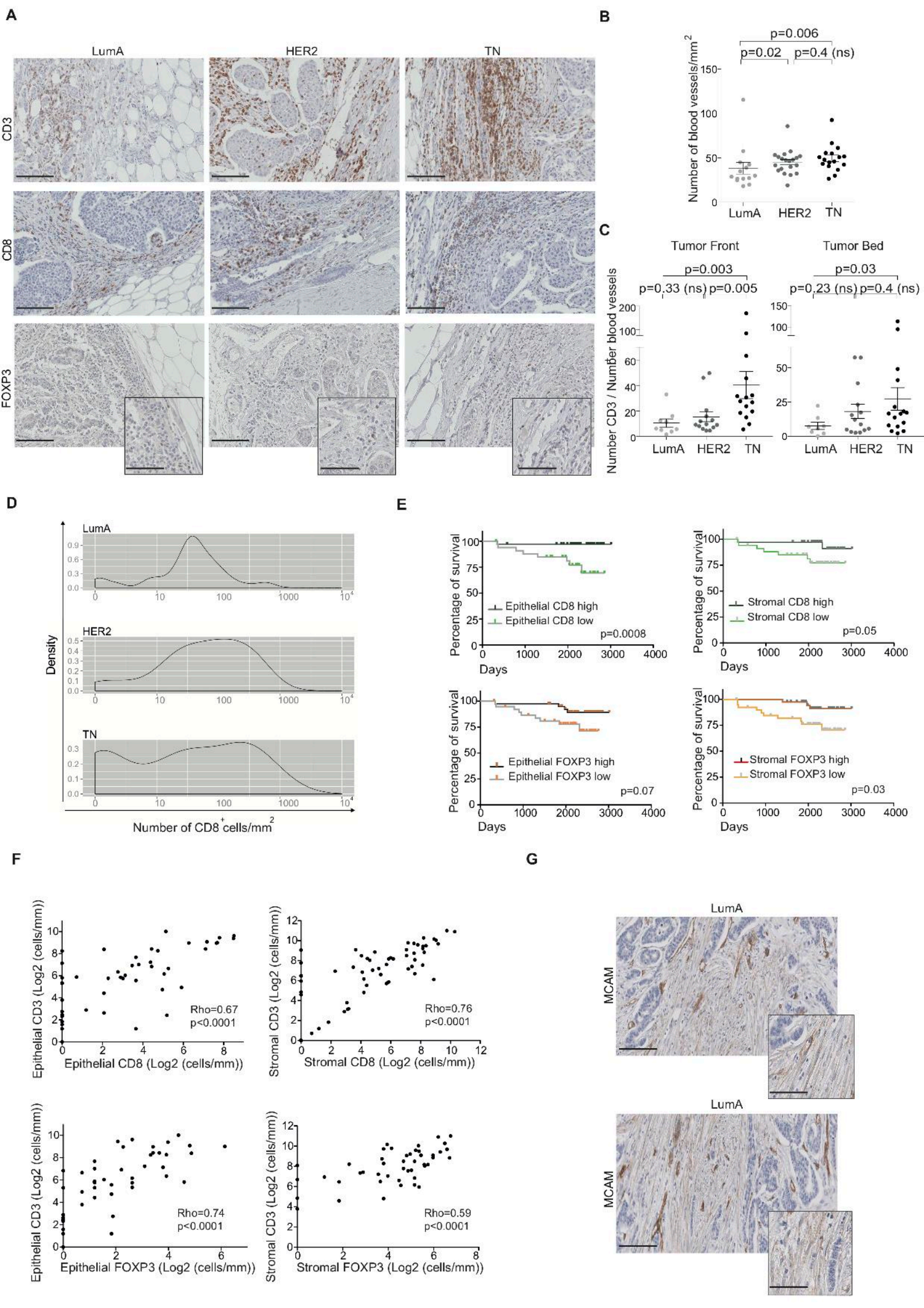
A
LumA
HER2
TN
CD3
CD8
FOXP3
B
p=0.006
p=0.02
p=0.4 (ns)
Number of blood vessels/mm2
LumA
HER2
TN
C
Tumor Front
Tumor Bed
p=0.003
p=0.33 (ns)
p=0.005
p=0.03
p=0.23 (ns)
p=0.4 (ns)
Number CD3 / Number blood vessels
LumA
HER2
TN
D
LumA
HER2
TN
Density
Number of CD8+ cells/mm2
E
Epithelial CD8 high
Epithelial CD8 low
p=0.0008
Stromal CD8 high
Stromal CD8 low
p=0.05
Epithelial FOXP3 high
Epithelial FOXP3 low
p=0.07
Stromal FOXP3 high
Stromal FOXP3 low
p=0.03
Percentage of survival
Days
F
Epithelial CD3 (Log2 (cells/mm))
Epithelial CD8 (Log2 (cells/mm))
Rho=0.67
p<0.0001
Stromal CD3 (Log2 (cells/mm))
Stromal CD8 (Log2 (cells/mm))
Rho=0.76
p<0.0001
Epithelial FOXP3 (Log2 (cells/mm))
Rho=0.74
p<0.0001
Stromal FOXP3 (Log2 (cells/mm))
Rho=0.59
p<0.0001
G
LumA
MCAM
LumA
MCAM

Figure S3. Tumor infiltrating lymphocytes, blood vessel assessment and MCAM staining in BC, Related to Figures 3 and 4.

(A) Representative views of $CD3^+$, $CD8^+$ and $FOXP3^+$ staining by IHC showing the tumor front of LumA, HER2 and TN BC subtypes. Scale bar = 100 µm, with 25 µm in inset.

(B) Scatter plot showing the number of blood vessels / mm^2 quantified by using $CD31^+$ staining in the tumor bed of LumA, HER2 and TN BC from the exploratory cohort. n = 60 BC (20 LumA, 19 HER2, 21 TN). Data are shown as mean ± SEM. p values are based on Mann-Whitney test.

(C) Scatter plots showing the $CD3^+$ TIL infiltration in BC normalized to the vessel content, given by the ratio of the number of $CD3^+$ T-lymphocytes / mm^2 to the number of blood vessels / mm^2 (defined by $CD31^+$ staining) in the tumor front (Left) and tumor bed (Right). Data are from the exploratory cohort (n = 60 BC; 20 LumA, 19 HER2, 21 TN) and are shown as mean ± SEM. p values are from Mann-Whitney test.

(D) Density plots showing the number of $CD8^+$ T lymphocytes per mm^2 by BC subtype. Data are shown in logarithmic scale.

(E) Kaplan-Meier curves showing TN BC patient overall survival according to the $CD8^+$ or $FOXP3^+$ T lymphocytes in tumor bed in stromal and epithelial compartments. Classes of TN BC patients with high (n = 34) or low (n = 35) $CD8^+$ or $FOXP3^+$ infiltration was determined using the median. p values are based on Log-rank test.

(F) Correlation between numbers of $CD8^+$ T lymphocytes / mm^2 and $CD3^+$ T lymphocytes / mm^2, on the one hand, and $FOXP3^+$ T lymphocytes / mm^2 and $CD3^+$ T lymphocytes / mm^2 on the other hand, as indicated. Quantifications in epithelial and stromal compartments are shown. Data are from the validation retrospective cohort. Correlation coefficients and p values are from Spearman's test.

(G) Representative views of MCAM/CD146 immunostaining in tumor bed of BC sections. Scale bar = 100 µm, with 25 µm in inset.

Table S5, Composition of the modules from the comprehensive CAF-specific map of molecular interactions, Related to Figure 4

Module	Gene
GROWTH FACTORS SIGNALING PATHWAYS	TGFB1, TGFB2, TGFB3, EGF, PDGFA, PDGFB, PDGFC, FGF2, HGF, SHH, IHH, GLI1, SMAD2, SMAD4, SMAD3, TGFBR2, TGFBR1, PGDFRA, PGDFRB, FGFR1, EGFR, ERBB2, ERBB3, ERBB4, MIF, CD74, WNT7, FKBP1A, SMURF1, ZFYVE9, LTBP1, LTBP2, LTBP3, LTBP4, TGFB, IGF2, MET, FRS2, IRS1, IGF2R, PTCH1, PTCH2, SMO, GLI2, GLI3, SMAD7, MIR21
INTEGRINS SIGNALING PATHWAYS	FN1, COL1A1, COL1A2, COL2A1, COL3A1, COL4A1, COL4A2, COL4A3, COL4A4, COL4A5, COL4A6, COL5A1, COL5A2, COL5A3, COL6A1, COL6A2, COL6A3, COL6A4P1, COL6A4P2, COL6A5, COL6A6, COL7A1, COL8A1, COL8A2, COL9A1, COL9A2, COL9A3, COL10A1, COL11A1, COL11A2, COL12A1, COL13A1, COL14A1, COL15A1, COL16A1, COL17A1, COL18A1, COL19A1, COL20A1, COL21A1, COL22A1, COL23A1, COL24A1, COL25A1, COL26A1, COL27A1, COL28A1, ITGA1, ITGB1, ITGA2, ILK, ITGB3, ITGAV, ITGB5, PTK2, SRC, ITGB6, ITGA3, ITGA11, ITGA5, LAMA1, LAMA2, LAMA3, LAMA4, LAMA5, LAMB1, LAMB2, LAMB3, LAMB4, LAMC1, LAMC2, LAMC3, VTN, RAB21, POSTN
MOTILITY	ACTA2, YAP1, ACTG2, CDC42, ROCK1, ROCK2, RHOA, MYH9, MYH10, MYH14, MYL9, MYL12A, MYL12B, MYL6, MYL6B, MYLK, MYLK2, CDC42BPA, CDC42BPB, PPP1R12A, PPP1CA, PPP1CB, PPP1CC, PPP1R12B, TUBA1A, TUBA1B, TUBA1C, TUBA3C, TUBA3D, TUBA3E, TUBA4A, TUBA8, TUBB, TUBB1, TUBB2A, TUBB2B, TUBB2C, TUBB3, TUBB4, TUBB4Q, TUBB6, ACTA1, ACTB, ACTC1, ACTG1, RAC1, RAC2, ARHGAP35, WAS, WASL, ARPC3, ARPC4, ARPC5, ACTR3, ACTR2, ARPC2, ARPC1A, ARPC1B, LIMK1, CFL1, WASF1, WASF2, WASF3, CDC42EP3
MATRIX REGULATION	FN1, MMP1, MMP2, MMP3, MMP7, MMP8, MMP9, MMP10, MMP11, MMP12, MMP13, MMP14, MMP15, MMP16, MMP17, MMP19, MMP20, MMP21, MMP23A, MMP23B, MMP24, MMP25, MMP26, MMP27, MMP28, LOX, COL1A1, COL1A2, COL2A1, COL3A1, COL4A1, COL4A2, COL4A3, COL4A4, COL4A5, COL4A6, COL5A1, COL5A2, COL5A3, COL6A1, COL6A2, COL6A3, COL6A4P1, COL6A4P2, COL6A5, COL6A6, COL7A1, COL8A1, COL8A2, COL9A1, COL9A2, COL9A3, COL10A1, COL11A1, COL11A2, COL12A1, COL13A1, COL14A1, COL15A1, COL16A1, COL17A1, COL18A1, COL19A1, COL20A1, COL21A1, COL22A1, COL23A1, COL24A1, COL25A1, COL26A1, COL27A1, COL28A1, HAS2, TIMP1, LAMA1, LAMA2, LAMA3, LAMA4, LAMA5, LAMB1, LAMB2, LAMB3, LAMB4, LAMC1, LAMC2, LAMC3, LOXL1, EMILIN2, TIMP2, POSTN, LOXL2, DPP4
GROWTH FACTORS PRODUCTION	TGFB1, TGFB2, TGFB3, EGF, PDGFA, PDGFB, PDGFC, FGF2, NGF, HGF, CTGF, VEGFA, BMP4, LTBP1, LTBP2, LTBP3, LTBP4, TGFB, IGF2, FGF7, STC1
MARKERS OF FIBROBLAST ACTIVATION	ACTA2, TNC, CSPG4, PDGFRB, FAP, PALLD, PDPN, S100A4, VIM, SPARC, CNN1, EDN1, MYL12A, TAGLN2, ACTG2, THY1, CYR61, CA9, HSF1
CYTOKINES AND CHEMOKINES PRODUCTION	CLL2, IL6, CCL5, CXCL14, IL1B, PTGS2, IL32, CLCF1, CCL7, CXCL12, IL17A, IL11, CXCL7, CXCL6, CXCL8, CCL20, IDO1, CXCL1, CCL3, CXCL2, TNF, CXCL5, TSLP, LIF, PLAU, CXCL9, CXCL10, CXCL11, CXCL17, IL15, CD274, PDCD1LG2, HLA-DMA, HLA-DMB, HLA-DOA, HLA-DOB, HLA-DPA1, HLA-DPB1, HLA-DQA1, HLA-DQA2, HLA-DQB1, HLA-DQB2, HLA-DRA, HLA-DRB1, HLA-DRB3, HLA-DRB4, HLA-DRB5, TNFSF4, CD276, IL13, CCL2
INFLAMMATORY SIGNALING PATHWAYS	FAP, SERPINE1, PLG, IL6, CXCL12, ILB1, IL1R, IL1RAP, IRAK1, TRAF6, IRAK4, MYD88, IL6ST, IL6R, JAK1, TYK2, JAK2, PTGER2, TNF, TNFRSF1A, TRADD, RIPK1, TRAF2, FADD, TRAF1, TNFRSF1B, PLAU, PLAUR, STAT3, STAT1, IL1A, BIRC2, BIRC3, RNF31, SHARPIN, RBCK1, OSM, LIF, LIFR, PTPN6, CXCR4
CORE SIGNALING	YAP1,WWTR1,SPP1,NFKBIA,NFKBIB,NFKBIE,RELB,RELA,CHUK,IKBKB,IKBKG,NFKB1,TAB3,TAB2,MAP3K7,PDK1,AKT1,AKT2,AKT3,GRB2,PIK3CA,PIK3CB,PIK3CD,PIK3CG,PIK3R1,PIK3R2,MAPK11,MAPK12,MAPK13,MAPK14,MAPK8,MAPK9,MAPK10,PTEN,CCDC88A,CREBBP,EP300,EGR1,MAPK3,MAPK1,ETS1,RAB21,PTPN6,ETS2,SOS1,SOS2,MAP2K1,MAP2K2,PTPN11,GAB1,SHC1,NRAS,KRAS,HRAS,RAF1,ARAF,BRAF,PLCG1,PRKCA,PRKCB,PRKCE,PRKCG,PRKCZ,PRKCD,PRKCH,PRKCQ,PRKCI,MTOR,RPTOR,MLST8,DEPTOR,AKT1S1,MIR21,PDPN,SERPINE1,SPARC,SIRT3,SMAD7,JAK1,JAK2,,RB1,TP53,CAV1,STAT1,IFNGR1,IFNGR2,IFNG,IGFBP3,IGFBP4,SERPINF1,JUND,IQGAP1,RBPJ,SQSTM1,CD80,SOD2,TFAM,MIR320A,MIR31,IGF2R,MIR149,IDH3A
MODULATORS OF REGULATORY T LYMPHOCYTES	TGFB1,TGFB2,TGFB3,CCL5, CXCL12,IDO1,VEGFA,TSLP,LTBP1,LTBP2,LTBP3,LTBP4,TGFB,CCL22,CCL28,CXCL9,CXCL10,CXCL11,CXCL17,IL2,IL15,IL7,TNFSF4,CD276
INTERACTION WITH TUMORAL CELLS	CCR3,CCL7,CCR1,MIR205,HSPA5,SLC16A1

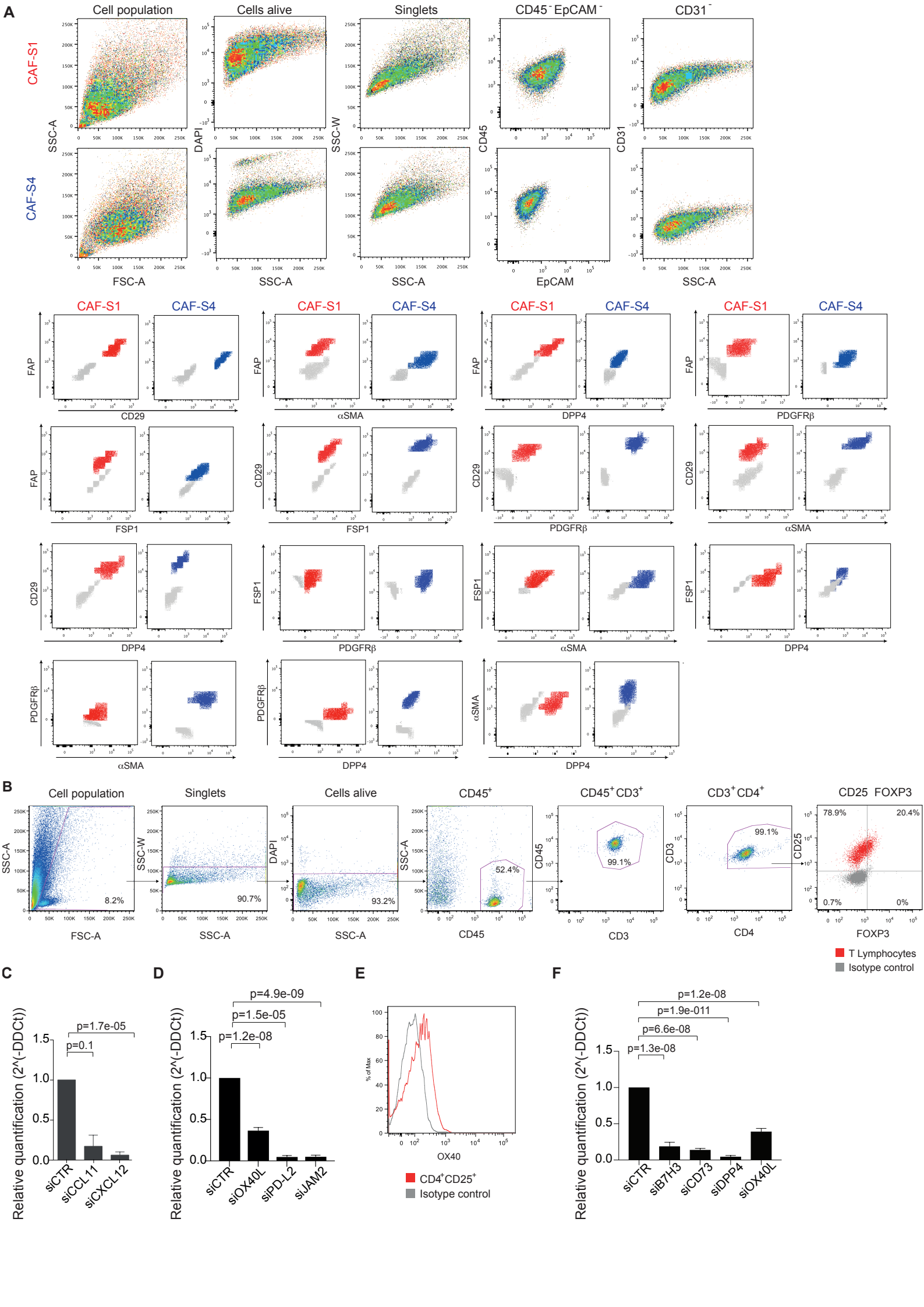
A
Cell population
Cells alive
Singlets
CD45- EpCAM-
CD31-
CAF-S1
CAF-S4
SSC-A
DAPI
SSC-W
CD45
CD31
FSC-A
SSC-A
EpCAM
FAP
CD29
αSMA
DPP4
PDGFRβ
FSP1
B
Cell population
Singlets
Cells alive
CD45+
CD45+CD3+
CD3+CD4+
CD25 FOXP3
8.2%
90.7%
93.2%
52.4%
99.1%
78.9%
20.4%
0.7%
0%
FSC-A
SSC-A
CD45
CD3
CD4
CD25
FOXP3
T Lymphocytes
Isotype control
C
Relative quantification (2^(-DDCt))
p=1.7e-05
p=0.1
siCTR
siCCL11
siCXCL12
D
p=4.9e-09
p=1.5e-05
p=1.2e-08
siCTR
siOX40L
siPD-L2
siJAM2
E
% of Max
OX40
CD4+CD25+
Isotype control
F
p=1.2e-08
p=1.9e-011
p=6.6e-08
p=1.3e-08
siCTR
siB7H3
siCD73
siDPP4
siOX40L

Figure S4. Monitoring the identity of CAF-S1 and CAF-S4 primary cell lines, isolation of $CD25^+$ T lymphocytes and validation of silencing efficiency, Related to Figures 5 and 6.

(A) Representative flow cytometry plots showing the gating strategy used to confirm the identity of CAF-S1 and CAF-S4 primary cells isolated from surgical BC and put in culture for use in functional assays. Cells were first gated on $DAPI^-$, singlets, $EPCAM^-$ $CD45^-$ and $CD31^-$, to exclude dead, doublets, epithelial, hematopoietic and endothelial cells, respectively (Top). Cells were next examined using 6 fibroblast markers. Representative gating using CD29, FAP, αSMA, FSP1, DPP4 (DPP4 marker was defined as specific of CAF-S1 from RNAseq data) and PDGFRβ markers is shown (Bottom). Representative flow cytometry plots for each marker in CAF-S1 and CAF-S4 primary sub-populations maintained in culture conditions are shown. In red are shown CAF-S1 fibroblasts, in blue CAF-S4 fibroblasts. Isotype control is shown in grey.

(B) Flow cytometry plots showing the gating strategy used to confirm the purity of the $CD4^+CD25^+$ T lymphocytes after isolation from one representative donor. Singlet cells were first gated on $DAPI^-$ $CD45^+$ $CD3^+$ $CD4^+$ and next examined using CD25 and FOXP3. The $CD4^+CD25^+$ T lymphocytes are shown in red and isotype control in grey.

(C) Barplot showing CCL11 and CXCL12 mRNA levels in CAF-S1 cells transiently transfected with a control- (siCTR), CCL11- (siCCL11) or CXCL12- (siCXCL12) targeted siRNA. mRNA levels were monitored by RT-qPCR. Data are shown as means ± SEM of fold change to the control condition (n = 2 and n = 5 independent experiments for CCL11 and CXCL12, respectively). p values are from one sample t-test.

(D) Same as in (C) for TNFSF4 (OX40L), PDCD1LG2 (PD-L2) and JAM2. n ≥ 4 independent experiments.

(E) Representative density curves showing the fluorescence intensity of OX40 (TNSFR4) expression at the surface of $CD4^+CD25^+$ T lymphocytes isolated from blood mononuclear cells of a healthy donor. Isotype control is shown in grey. Data are expressed as percentages of maximal number of cells (% of Max).

(F) Same as in (C) for CD276 (B7H3), NT5E (CD73), DPP4 and TNFSF4 (OX40L). n ≥ 6 independent experiments.